# 1 Hyperspectral mapping of density, porosity, stiffness, and strength in

# 2 hydrothermally altered volcanic rocks

- 3 Samuel T. Thiele<sup>1</sup>, Gabor Kereszturi<sup>2</sup>, Michael J. Heap<sup>3,4</sup>, Andréa de Lima Ribeiro<sup>1</sup>, Akshay Kamath<sup>1</sup>,
- 4 Maia Kidd<sup>2</sup>, Matías Tramontini<sup>5</sup>, Marina Rosas-Carbajal<sup>6</sup>, Richard Gloaguen<sup>1</sup>
- 6 <sup>1</sup>Helmholtz-Zentrum Dresden-Rossendorf, Helmholtz Institute Freiberg, Chemnitzer Str. 40, 09599 Freiberg, Germany
- 7 <sup>2</sup>Volcanic Risk Solutions, School of Agriculture and Environment, Massey University, Palmerston North, New Zealand
- 8 <sup>3</sup>Université de Strasbourg, CNRS, Institut Terre et Environnement de Strasbourg, UMR 7063, 5 rue Descartes, Strasbourg
- 9 F-67084, France

- 10 <sup>4</sup>Institut Universitaire de France (IUF), Paris, France
- 11 <sup>5</sup>CONICET Facultad de Ciencias Astronómicas y Geofísicas, Universidad Nacional de La Plata, Argentina
- 12 <sup>6</sup>Université de Paris Cité, Institut de Physique du Globe de Paris, CNRS, F-75005 Paris, France
- 13 Correspondence to: Samuel T Thiele (s.thiele@hzdr.de)
- Abstract. Heterogeneous structures and diverse volcanic, hydrothermal, and geomorphological processes hinder the characterisation of the mechanical properties of volcanic rock masses. Laboratory experiments can provide accurate rock property measurements, but are limited by sample scale and labor-intensive procedures. In this contribution, we expand on 17 previous research linking the hyperspectral fingerprints of rocks to their physical and mechanical properties. We acquired a 18 unique reflectance dataset covering the visible-near infrared (VNIR), shortwave infrared (SWIR), midwave infrared 19 (MWIR), and longwave infrared (LWIR) of rocks sampled on eight basaltic to andesitic volcanoes. We trained several 20 machine learning models to predict density, porosity, uniaxial compressive strength (UCS), and Young's modulus (E) from 19 the spectral data. Significantly, nonlinear techniques such as multilayer perceptron (MLP) models were able to explain up to 19 20 80% of the variance in density and porosity, and 65–70% of the variance in UCS and E. Shapley value analysis, a tool from 19 21 explainable AI, highlights the dominant contribution of VNIR-SWIR features that can be attributed to hydrothermal 24 alteration and MWIR-LWIR features witnessingsensitive to volcanic glass content and, likely, fabric and/or surface 25 roughness. These results demonstrate that hyperspectral imaging can serve as a robust proxy for rock physical and 26 mechanical properties, potentially offering an efficient, scalable method for characterising large areas of exposed volcanic 27 rock. The integration of these data with geomechanical models could enhance hazard assessment, infrastructure 28 development, and resource utilisation in volcanic regions.

# 30 1 Introduction

32 Toth, 2021; Soltani et al., 2019) and critical raw materials (Lewicka et al., 2021). Simultaneously, population growth and 33 increasingly extreme weather (Aubry et al., 2022; Farquharson et al., 2015) expose a growing number of people to 34 geological hazards, including rock falls, landslides, and volcanic eruptions. Effective management of these resources and 35 hazards requires detailed characterisation of the subsurface geology, its physical properties (e.g., density and permeability). 36 and its mechanical behaviour (e.g., strength and deformability). 37 Volcanic regions commonly host mineral, water, and geothermal resources, and are also extremely prone to geological 38 hazards. However, the mechanical behavior of volcanic rock masses remains challenging to characterize, due to the diverse 39 volcanic, hydrothermal, sedimentological and geomorphological processes that shape and reshape them (Heap and Violay, 40 2021). Although mechanical properties can be accurately and routinely measured in the laboratory, samples are typically 41 limited to the centimeter- to decimeter-scale, which is several orders of magnitude smaller than is required to predict surface 42 deformation or reservoir behavior. Obtaining sufficient measurements to statistically characterize large-scale mechanical 43 variability thus remains a challenge, given the laborious mechanical tests required to measure e.g., strength, stiffness, and 44 hydraulic properties. 45 Several proxy measures have been developed to help mitigate sampling limitations, including field measurements of porosity 46 and permeability (Farquharson et al., 2015; Mordensky et al., 2018), Schmidt hardness (del Potro and Hürlimann, 2009; 47 Dincer et al., 2004; Harnett et al., 2019; Mordensky et al., 2018), point-load strength (Poganj et al., 2025), reflectance 48 spectroscopy (Kamath et al., 2025; Bakun-Mazor et al., 2024; Kereszturi et al., 2023; Schaefer et al., 2021), and thermal 49 inertia (Franzosi et al., 2023; Loche et al., 2021; Mineo and Pappalardo, 2016). These proxies are easier to obtain than many 50 mechanical test results, and often correlate well with important laboratory-measured properties like strength and stiffness 51 after calibration for specific geological contexts or settings. 52 Hyperspectral reflectance data could provide an especially useful proxy for mechanical properties, as they can be collected 53 rapidly and, potentially, acquired remotely using imaging sensors. This approach could make use of the latent influence that 54 lithological properties like mineralogy, fabric, and porosity have on both the hyperspectral and mechanical response. For 55 instance, Schaefer et al. (2021) used visible-near (VNIR; 350-900 nm) and shortwave (SWIR; 900-2500 nm) infrared 56 reflectance spectroscopy to correlate spectral features and mineralogy with porosity and strength, and identified moderate 57 Spearman rank correlation with 390, 2207, and 2325 nm features. Kereszturi et al. (2023) also used VNIR and SWIR 58 hyperspectral data to predict porosity and unconfined compressive strength (UCS) in volcanic rocks, explaining 40–50% of 59 the mechanical variance. Lee et al. (2023) applied VNIR, SWIR, and midwave infrared (MWIR; 3000-5200 nm) data to 60 predict the dynamic elastic moduli of finely laminated shales, with R<sup>2</sup> scores between 0.4 and 0.8, but across a small sample 61 set. Most recently, Bakun-Mazor et al. (2024) used VNIR-SWIR and longwave infrared (LWIR; 7000–12000 nm) spectra to 62 estimate several mechanical properties, including UCS, in carbonate rocks, with generally high (0.8 to 0.9) R<sup>2</sup> scores.

31 Society is dependent on subsurface resources, including groundwater (Foster et al., 2013), low-carbon energy (Lund and

- 63 However, further research is needed to understand the relationships between hyperspectral data and the mechanical
- 64 properties of volcanic rocks, due to their complex microstructures and mineralogies, as well as the impact of hydrothermal
- 65 alteration.
- 66 In this contribution we investigate the relationships between hyperspectral data and the mechanical properties of volcanic
- 67 rocks, specifically focusing on density, porosity, UCS, and Young's modulus (E). E is of particular interest, as it has not
- 68 previously been linked to hyperspectral data and is crucial to predict surface deformation occurring during e.g. construction
- 69 or tunnelling works, mining, and volcanic unrest (Arens et al., 2022; Harnett and Heap, 2021; Heap et al., 2020b, 2021b;
- 70 Hickey et al., 2022; Hoek and Diederichs, 2006; Strehlow et al., 2015; Vrakas et al., 2018).
- 71 We therefore expanded the dataset presented by Kereszturi et al. (2023) to include samples from more volcanoes, and cover
- 72 an extended spectral range (VNIR-SWIR-MWIR-LWIR). This dataset is then leveraged to:
- 1. Train machine learning models to predict density, porosity, UCS, and E.
- Identify hyperspectral indicators for hydrothermal alteration, and explore how these are linked to the measured and
   predicted mechanical properties.
- Quantify the influence of different spectral ranges on each predicted property, to explore the spectral features that
   inform our model.
- 78 By advancing our understanding of the correlations between hyperspectral and mechanical properties, we ultimately aim to
- 79 improve our ability to characterise complex and heterogeneous volcanic rock masses.

#### 80 2 Theory

#### 81 2.1 Light-matter interactions: reflection and scattering

- 82 Light-matter interactions are complex, and governed by multiple interacting optical phenomena. Reflectance is a remotely
- 83 measurable, dimensionless expression of these interactions, defined by the ratio between the excitation signal (illumination
- 84 or irradiance, W.m-2) and signals emitted back towards a sensor (radiance, W.m-2.sr-1). Hyperspectral sensors measure this
- 85 returned radiance, and split it into many narrow but contiguous wavelength ranges to derive a radiance spectra that, after
- 86 correction to derive reflectance, contains information on the target material.
- 87 Links between hyperspectral reflectance spectra and mineralogy are well established, as reviewed by Laukamp et al. (2021)
- 88 and Williams and Ramsey (2024). Specific spectral ranges can be used to identify certain elements, due to the absorption of
- 89 VNIR range light during electronic transitions in metals like Fe, and covalent bonds that absorb energy at specific
- 90 wavelengths by stretching and bending activity. Compounds containing O-H, C-O and S-O bonds tend to have diagnostic
- 91 absorption features in the SWIR and MWIR ranges, while stretching and bending vibrations of Si-O bonds cause absorption
- 92 in the upper MWIR and LWIR ranges.
- 93 In volcanic contexts, electronic transition absorptions in the VNIR range can be used to detect common Fe3+ and Fe2+ rich
- 94 minerals, including hematite, goethite, and jarosite. SWIR range data are sensitive to hydroxylated silicates, including clay

96 for hydroxylate silicate and carbonate minerals. Finally, the upper MWIR and LWIR range is strongly influenced by 97 absorptions from the Si-O bonds in silicate minerals and glasses, and can be used to characterise the extent of silica 98 polymerization and to identify most rock-forming silicates (e.g., quartz, feldspars, pyroxene). 99 Regardless of the spectral range, features observed in reflectance spectra are determined by a combination of refraction, 100 absorption and scattering characteristics inherent to each material, and abide by Snell's law (Kirkland et al., 2003; Rost et al., 101 2018). The expected positions of absorption features are well-established, including subtle variations caused by differences 102 in crystal structure that often allow precise identification of specific minerals (Laukamp et al., 2021). However, spectral 103 characteristics like overall albedo, broad fluctuations in reflectance intensity, and the depth and asymmetry of absorption 104 modes (spectral contrast), can vary significantly between rocks with the same mineralogy. These wavelength-dependent 105 variations derive from processes occurring as light interacts with the surface of a rock and while traveling through its solid 106 constituents (and pore spaces), carrying information linked to surface and bulk physical properties. For consistency, we refer 107 to changes in the direction and intensity of light which are directly dependent on the surface characteristics as 'surface 108 scattering', and as 'volume scattering' when these changes are linked to processes occurring below the surface. Accordingly, 109 light-matter interactions in natural minerals can be understood through the combination of two optical scattering 110 components: surface and volume (Osterloo et al., 2012; Rost et al., 2018; Vincent and Hunt, 1968). 111 Surface scattering occurs when light interacts mostly with the superficial layer of a mineral, which acts as a mirror-like 112 interface and reflects light without transmitting it to the internal constituents of a rock (hereafter referred to as grains, 113 although we use this term inclusively of crystals, clasts and fragments) (Fig. 1a). This happens when the extinction 114 coefficient of light in a medium (k) is larger than its refractive index (n); as most of the incident radiation is absorbed at the 115 surface and not transmitted to higher depths (Hardgrove et al., 2016). The magnitude of surface scattering can vary with 116 wavelength (as n and k are both wavelength dependent), and is highly sensitive to the scale of surface topography relative to 117 the wavelength (Rayleigh's criterion; Hapke, 2012, 1981). A surface is considered perfectly smooth when its average 118 roughness is smaller than the wavelength of the incident light, with the outcoming light being reflected at the same angle as 119 the incoming radiation. This phenomenon, known as specular reflection, is particularly important in the LWIR region 120 (5,000–50,000 nm) (Fig. 1a). As roughness increases, surface irregularities serve as points for the incoming light to scatter 121 into several directions, spreading the total reflected energy in a Lambertian-like process known as diffuse scattering (Fig. 122 1a). Diffuse scattering is particularly important in the VNIR-SWIR analysis of rough surfaces in which asperities are 123 oriented towards different directions. In extreme cases, multiple diffuse patterns can occur within a small area, leading to a 124 multi-path scattering pattern (Fig. 1a). 125 In addition to impacting surface scattering, increased roughness enhances the transmission of incoming light through grains 126 at the sample surface, even when k is larger than n. This process, known as volume scattering, introduces longer paths and 127 changes in direction for light travelling within the medium leading to partial energy loss and reduced spectral contrast

95 minerals, sulphates, and carbonates. The MWIR range is less widely used, but also includes diagnostic absorption features

128 (Kirkland et al., 2003, 2001; Osterloo et al., 2012; Rost et al., 2018) due to light undergoing absorption within the medium

130 observed especially in the presence of smaller grains (Hunt and Vincent, 1968; Lyon, 1965; Mustard and Hays, 1997; 131 Salisbury and Wald, 1992). It is important to note that although the impact of volume scattering on the reflectance spectrum 132 is dependent on the inherent optical properties of the mineral, roughness, and the wavelength of the incoming light, these 133 relationships are highly non-linear and difficult to characterise for real multi-phase materials (i.e. rocks). In the LWIR, both 134 increased and decreased spectral contrast have been associated with volume scattering, highlighting the complexity of these 135 interactions (Osterloo et al., 2012). 136 For most real materials and mineral mixtures, both surface and volume scattering influence the reflectance spectra, with 137 different contributions depending (again) on the surface roughness, grain size, and wavelength range. An exemplary case of 138 surface and volume processes acting simultaneously is encountered for porous materials (Fig 1e). Pore size, shape and 139 distribution are directly linked to surface roughness, impacting the light-matter interaction dynamics by: i) enhancing the 140 volume scattering by transmitting light through interfaces barriers regions with different k and n (e.g. mineral/air/mineral 141 interfaces), leading to longer travel paths; and ii) by trapping light at pores with high depth-to-width ratios, causing multiple 142 surface reflection paths (cavity effect) and, in extreme cases, leading to total absorption of light before it can be reflected out 143 of the cavity (Hardgrove et al., 2016; Huang et al., 2021; Kirkland et al., 2001). Ultimately, increased porosity may lead to 144 important changes in the reflectance spectrum, particularly in the thermal region (5,000–50,000), and is associated with 145 reduced spectral contrast and inhibition of diagnostic mineralogical absorption features (Osterloo et al., 2012; Rost et al., 146 2018; Salisbury and Eastes, 1985).

129 prior to being scattered back to the surface (Fig. 1d). Increased volume scattering is also linked to the grain size, and

#### 147 2.2 Hapke's model

148 Hyperspectral cameras operate as fixed-position external-reflectance sensors, collecting the radiation scattered in a specific 149 direction from a material excited by a light source of known characteristics. Hence, material properties which affect the 150 amount of radiation scattered towards a detector influence the measured spectra. Several models (broadly known as the 151 Hapke model) have been proposed to investigate these light-mineral interaction dynamics, initially in the context of 152 extraterrestrial remote sensing (Hapke, 2012, 2008, 2002, 1984, 1981). Hapke's models aim to estimate bidirectional 153 reflectance signals collected by external-reflectance sensors. They are based on radiative transfer theory and on the works 154 from Chandrasekhar (1960), and form an important theoretical basis for hyperspectral imaging applications. The core 155 premise of Hapke's models is that reflectance spectra can be parameterised as a function of material type and morphological 156 properties (Hapke, 1993).

157 While a detailed examination of Hapke's model(s) is beyond the scope of this contribution, we aim here to identify several 158 key elements that link reflectance signals with roughness, grain size and porosity. These effects are highlighted using the 159 following formula,

160 
$$r(i,e,\alpha,\lambda) = K \frac{\omega(\lambda)}{4} \left( [1 + B(\alpha)] P(\alpha) + M(i,e,\alpha,\lambda) - 1 \right),$$

161 <del>(1)</del> (Eq. 1),

162

where  $r(i,e,\alpha,\lambda)$  is the scattering intensity (radiance); K is the filling factor (linked to porosity; Hapke, 2008);=  $\omega$  ( $\lambda$ =) is the 164 average single scattering albedo (SSA; linked to absorption and scattering at particle level and dependent on the wavelength 165  $\lambda$ );  $B(\alpha)$  is the opposition surge function (Hapke, 1993, 1986);  $P(\alpha)$  is the average single scattering function for the phase 166 angle  $\alpha$ ;— i and e are the angles of incidence and emission;  $M(i,e,\alpha,\lambda^{-})$  represents the wavelength-dependent multiple 167 scattering effect (MSE). It is important to note that Hapke's refers to 'scattering' as an integration of all radiation emitted by 168 a surface following interactions with an excitation source, with no distinction between surface and volume processes. 169 Instead, the models provide a holistic approach in which multiple terms are influenced by both surface and volume 170 processes. In this context, radiance is thus the total signal scattered by an object towards a detector. In hyperspectral remote 171 sensing, the distinction between surface and volume scattering contributions is important, as surface and subsurface rock 172 characteristics are linked to changes in the reflectance spectra (cf., section 2.1).

173

The single and multiple scattering terms (SSA and MSE) are the primary contributors to the reflectance estimated by the model. Whilst SSA represents the probability of light being scattered or absorbed by a single grain, MSE (derived from Ambartsumian-Chandrasekhar H-function and dependent on SSA) accounts for multiple scattering prior to its emission towards a detector. Both parameters are material-specific, and vary according to changes in roughness, grain size, and wavelength of light. Another core term is the phase function  $P(\alpha)$ , which estimates how much light is scattered in a given direction relative to the direction of incoming light as a function of the angle between the illumination direction and the viewing direction (phase angle,  $\alpha$ ). The intensity and direction of the phase function are not material-specific, but— $\alpha$  also linked to  $\alpha$ , and introduces a surface brightening effect as—it decreases (Hapke, 2002). Finally, the porosity parameter K accounts for changes in scattered signals due to increasing porosity and/or decreasing density (Hapke, 2008).

184

186 and sample roughness, grain size, porosity and composition. It is based on radiative transfer theory and traditionally used to 187 describe the scattering of light by planetary surfaces. It estimates the bidirectional reflectance of a surface, considering both 188 single and multiple scattering of light. The model can be tuned for specific applicationapplications, and generally 189 incorporate parameters such as single-scattering albedo, phase function, and surface roughness which have a 190 direct impact on the bidirectional reflectance signals. Hapke's model is therefore a strong basis for understanding the 191 interaction of light with rock surfaces, aiding in the interpretation of remote sensing data. While the complexity of real 192 samples typically limits the model's practical application, it provides a useful theoretical framework that will help us to 193 understand and interpret hyperspectral reflectance spectra.

# 195 3 Methods

# 196 3.1 Sample database

197 For this study, we compiled a new database of individual,332 well-characterised core samples that have been subjected to 198 laboratory rock deformation experiments (Heap et al., 2021a, 2020a; Leiter et al., 2024; Schaefer et al., 2023; Tramontini et 199 al., 2025; Vairé et al., 2024). These samples were collected in the scope of previous studies from eight basaltic to rhyolitic 200 composite volcanoes, including Cracked Mountain (Canada; Leiter et al., 2024), Ruapehu (New Zealand; Schaefer et al., 201 2023), La Soufrière de Guadeloupe (Eastern Caribbean; Heap et al., 2021b, 2021a), Ohakuri (New Zealand; Heap et al., 202 2020a), Chaîne des Puys (France; Vairé et al., 2024), Copahue (Argentina/Chile; Tramontini et al., 2025), Tongariro (New 203 Zealand; Kidd et al., 2025), and Whakaari (New Zealand; Kidd et al., 2025). 204 Most of the sampled rocks are basaltic to andesitic in composition, and cover a range of textures (breccias, pyroclastic, and 205 coherent lava rocks). A breadth of hydrothermal alteration is also covered, ranging from dominantly fresh rocks (e.g., from 206 Chaîne des Puys; Vairé et al., 2024) through to intense hydrothermal alteration (e.g., some samples from Ruapehu and 207 Whakaari; Schaefer et al., 2023). Altered samples in our sample set were subject to acid-sulphate related mineralogical 208 changes, including the formation of sulphates (e.g., jarosite, alunite and anhydrite), phyllosilicates (e.g., kaolinite and 209 montmorillonite), and various polymorphs of quartz (Heap et al., 2021a; Kereszturi et al., 2020). This diversity of alteration 210 is intended to help our machine learning models to learn some of the alteration systematics and capture how these can 211 influence the physical and mechanical properties of volcanic rocks.

# 212 3.2 Laboratory testing

214 were either performed at University of Strasbourg (France) or University of Canterbury (New Zealand). Prior to testing, the 215 samples were dried in a vacuum oven at 40 °C for a minimum of 48 hours (Strasbourg) or oven-dried at 60 °C for a 216 minimum of 48 hours (Canterbury). Dry bulk density was calculated using the dry mass and bulk volume of each sample. 217 Connected porosity was calculated using the skeletal volume, measured using an AccuPyc II 1340 pycnometer (Strasbourg 218 and Canterbury), and the bulk volume of each sample. 219 Uniaxial compressive strength (UCS) experiments were performed using a uniaxial load frame supplied by Schenk 220 (Strasbourg) or a 3000 kN Technotest uniaxial load frame (Canterbury). All experiments were performed on dry samples at 221 ambient laboratory temperatures. Samples were deformed at a constant strain rate of 10-5 s-1 until macroscopic sample

213 Mechanical test cores were prepared with a diameter of 20 mm and a length of ca. 40 mm. Measurements and experiments

222 failure (Fig. 2a). Axial displacement and axial force were measured by a linear variable differential transducer and a load 223 cell, respectively, and were converted to axial strain and axial stress using the initial length and radius of the sample, 224 respectively. More information, as well as schematic diagrams of the devices, can be found in Heap et al. (2014) and

225 Mordensky et al. (2018).

First, the maximum stress of each loading curve was identified as the UCS. The pre-failure loading curve was then smoothed slightly using a Savitzky–Golay filter and resampled to regular stress increments using a linear interpolation. The slope of the most linear part of the resampled loading curve was then identified to calculate E, using the random sample and consensus (RANSAC) algorithm. This regression technique robust to outliers iteratively fits data with a function (in this case linear) using random minimal subsets (two points) and maximises the number of inliers within a threshold distance. This approach successfully identifies the linear part of each loading curve while remaining robust to outliers caused by pre-failure inelastic deformation by maximising the number of inliers (rather than minimising residuals as per e.g., least-squares regression, Fig. 2c), allowing robust and objective measurement of E.

234 ¶

## 235 3.3 Hyperspectral data acquisition

A total of 332 individual core samples were compiled from eight basaltic to andesitic volcanoes and The core samples were arranged on non-reflective sample trays (Fig. 2a). These samples were, grouped by size to limit focal blur, leveled and fixed in place using plasticine and leveled to reduce illumination artifacts. Each tray was then scanned using a Specim SiSuROCK drill core scanner, which contains Specim AisaFENIX, FX50 and AisaOWL hyperspectral sensors and a high spatial Specim RGB-Jai camera (Fig. 2b). The workflow described by Thiele et al. (2024) was used to coregister data from each of the sensors and to convert from measured radiance to relative reflectance.

Each sample was then extracted from the coregistered stack of hyperspectral (and RGB) imagery using napari-hippo (Thiele et al., 2024), and stored as a separate set of images. The spectra of each image was smoothed slightly with a Savitzky–Golay filter (using a 1st order polynomial and window size of 5 bands), and hull-corrected using hylite (Thiele et al., 2021) to amplify spectral absorption features and reduce illumination artifacts caused by non-planar sample geometries. VNIR to MWIR spectra were corrected using an upper hull correction, while a lower hull correction was applied to the LWIR range data.

248 Median spectra from each mechanical test sample were then compiled into a spectral library covering the 249 VNIR-SWIR-MWIR-LWIR range. These were combined with the corresponding mechanical property measurements to 250 derive a training dataset.

Their mineralogy was characterised by indices extracted from the spectra of each sample using the minimum wavelength mapping approach (van der Meer et al., 2018) implemented in hylite (Thiele et al., 2021). These indices (Table 1) quantify specific spectral absorptions resulting from vibrational and bending vibrations associated with water, sulfate, hydroxylated phyllosilicates, and silicate minerals (Laukamp et al., 2021; Schodlok et al., 2016). Two composite indices were also calculated, to characterize bulk-composition and the extent of hydrothermal alteration. The first is the Mafic-Felsic Index of Schodlok et al., (2016), which distinguishes samples with basaltic compositions from those that are more evolved. This index, hereafter referred to as MFI, was computed by applying a lower-hull correction to the LWIR spectra between 7640 and 10620 nm and identifying the general position (wavelength) of the reflection peak within this range, using the

259 polynomial fitting approach implemented in hylite (Thiele et al., 2021). The results were then normalized to range between 0

260 (maxima at 10620 nm, indicating mafic compositions) and 1 (maxima at 7640 nm, indicating felsic compositions).

261 The second bulk index was derived by averaging the H2O and OH absorptions at ~1900 and 1400 nm (Table 1), to track the

262 total amount of water (as H2O, in e.g. quartz-hosted fluid inclusions, and as -OH groups in e.g., clay minerals). Because

263 most of the measured volcanic rocks are initially dry (with some exceptions, e.g., phreatomagmatic tuff), this water often

264 indicates hydrothermal alteration. We thus use this index as a rough proxy for hydrothermal alteration (and weathering)

265 processes. The presence of hydrated (alteration) minerals has been shown to correlate with mechanical response (Heap et al.,

**266** 2022).

267

# 268 3.4 Regression models

269 Each target variable (density, porosity, UCS, and E) requires transformation prior to model fitting, to reduce skew (Fig. 3)

270 and ensure the back-transformed predictions are correctly scaled (non-negative and, in the case of porosity, between 0 and 1).

271 A square root transform (Fig. 3e) was found to perform better than a log-transform (Fig. 3f), likely as it resulted in more

272 normally distributed data. Porosity was converted to a ratio of voids to solids (1 - porosity) prior to the square root transform,

273 mitigating challenges fitting regressions to closed data.

274 We ensure a robust calibration/validation by defining five folds using a stratified split with respect to porosity, to ensure that

275 each fold contains diverse mechanical properties. Several machine learning approaches (lasso regression, partial least square

276 regression, support vector regression, and multilayer perceptron regression), known to be adapted to this genre of tasks,

277 were then evaluated using the R2 metric and 5-fold cross validation (to account for potential overfitting). Model

278 hyperparameters were optimised to maximise the training R2 score, as documented in the Jupyter notebooks included in the

279 supplementary material. Finally, the best models Five models of each type were trained, each setting aside a single fold (20%)

280 of the data) as a test set. Each trained model was then used to predict its unseen test-set, and the results compiled for a robust

281 assessment of model accuracy. Finally, the best performing models (of different types) were combined into an ensemble,

282 allowing the prediction variance to be used as a measure of uncertainty.

#### 283 3.5 SHAP analysis

284 Shapley values (Shapley, 1973) have recently been adapted to help understand the predictions made by deep learning

285 models. Based on cooperative game theory, Shapley values quantify the contribution of individual features to output

286 predictions, providing a theoretically grounded measure of the average marginal contribution of each input feature across all

287 possible feature subsets (Lundberg and Lee, 2017). This allows a more detailed interpretation than other explanation

288 approaches, and in this case helps link model predictions to specific hyperspectral bands.

289 We used the python package SHAP (Shapley Additive Explanations; Lundberg and Lee, 2017) to compute Shapley values

290 for our ensemble models. Due to the various types of models included in these ensembles, a stochastic estimation approach

291 (KernelSHAP) was used. KernelSHAP is a model-agnostic algorithm that estimates Shapley values by systematically 292 perturbing input variables and measuring the resulting changes. The perturbative nature of this algorithm makes it 293 computationally expensive, requiring us to compute Shapley values only for a subset of our test dataset. This subset was 294 selected using k-means clustering, such that 16 representative data points (cluster centroids) could be selected for use by the 295 Kernel Explainer.

#### 296 4 Results

#### 297 4.1 Spectral response of hydrothermal alteration

298 A comparison of MFI, a proxy for composition, and hydration index, a proxy for hydrothermal alteration, highlights the 299 spectral diversity of our dataset (Fig. 4). Two broad populations of basalt (lower) and andesite (upper) form clear horizontal 300 "bands", each of which contains variable amounts of hydration. The MFI results broadly match the expected composition of 301 each volcano, albeit with exceptions including two altered samples from Whakaari with anomalously low MFI (due to the 302 confounding influence of non-silicate alteration minerals like jarosite or sulphur, rather than a mafic composition). 303 Diagnostic absorption features for kaolinite ( $v+\delta M2OHo$ ) and other clay minerals ( $v+\delta (A1)-OH$  and  $v+\delta (Mg)-OH$ ) are 304 prominent in many altered samples. Of these, the kaolinite-rich samples (Fig. 4e) tended to be associated with deeper 2vSi-O 305 absorptions in the MWIR range (at  $\sim$ 4500 nm and indicative of silicification) or  $\delta$ S-O absorptions in the SWIR range (at 306 ~1750 nm), indicating silicification and/or the presence of sulphate minerals like jarosite and alunite. In combination, these 307 spectral features indicate advanced argillic alteration, and are mostly associated with higher (andesitic) values of MFI (as our 308 dataset currently lacks basaltic examples of advanced argillic alteration). 309 Many samples also contain well defined  $v+\delta(Al)$ -OH absorption features (Fig. 4a), but without the previously mentioned 310 kaolinite, sulphate, or quartz-related absorption features. These are indicative of illite and smectite group clay minerals 311 formed by lower-temperature (<120° C) and/or higher pH hydrothermal alteration or weathering. Many of the basaltic 312 samples (lower MFI) also contain distinctive v+ $\delta$ (Mg)OH absorption features at 2300 nm, while lacking the v+ $\delta$ (Al)-OH 313 feature (Fig. 4b). We interpret this as either primary Al-poor clays (e.g., in palagonite tuffs), or as the result of argillic 314 alteration or weathering in Al-poor primary lithologies to form Fe- and Mg- rich clay minerals, like nontronite and hectorite. 315 Notably, all samples with spectral absorptions indicative of hydrothermal alteration also had prominent vOH and 316 vOH+ $\delta$ H2O absorptions at ~1400 and 1900 nm. This suggests that these combined features (our hydration index) can be 317 used to broadly quantify the intensity of hydrothermal alteration, because primary volcanic lithologies tend not to contain 318 hydrated or hydroxylated phases. Samples with higher hydration indices tended to be less dense (Fig. 5a) and have lower 319 UCS and E (Fig. 5c-d) than counterparts with lower hydration indices. Porosity showed a more complex relationship to the 320 hydration index (Fig. 5b), with a distinctive set of highly porous but non-hydrated samples (vesiculated lavas), and highly **321** porous and hydrated samples.

## 322 4.2 Rock property prediction

- The tested machine learning models gave a wide range of prediction accuracies, with highly varied 5-fold cross-validation R2 scores (Table 2). Linear models (PLSR and Lasso) performed poorly, suggesting a highly non-linear relationship between spectral response and rock properties (Table 2). Support Vector Regression (SVR) and Multilayer Perceptron (MLP) models were able to learn the nonlinear relations, yielding 5-fold cross validated R2 scores between 0.5 and 0.85 for each of the rock properties. Deeper multilayer perceptrons (with 8 to 16 fully connected layers) performed best. The need for depth further emphasises the need to capture nonlinear links in the underlying data structure and modelling.
- 329 Models fit to principal component (PCA) transformed inputs (retaining 25 independent features), including the MLP models 330 that theoretically work well with high-dimensionality input, performed better than models fit directly to concatenated 331 spectra.
- 332 No substantial difference in accuracy was observed between MLP models predicting a single output (i.e. univariate MLP 333 models that predict a single rock property) and multivariate MLP models (that predict each of the four rock properties 334 together). Ensemble predictions computed by averaging outputs from a set of nine manually selected (best-performing) SVM 335 and MLP models show similar or slightly improved R2 scores (relative to the individual models). However, these ensemble 336 models allow an estimate of prediction uncertainty (Fig. 6), based on the standard deviation ( $\sigma$ ) of the individual model 337 predictions. In most cases the measured rock property was within  $2\sigma$  of the ensemble mean, though several notable outliers 338 can also be identified. These include the prominently under-predicted UCS for one sample from Ruapehu (156 rather than 339 380 MPa), and over-estimated E for several samples from Ruapehu and Whakaari.
- 340 Interestingly, models trained and tested on the basaltic samples achieved higher R2 scores than equivalents trained and tested 341 on andesitic ones (Table 2). This implies that the rock properties of basalts (in our dataset) were easier to predict than 342 andesites, possibly due to the variability of the hydrothermally altered andesite relative to the basalts (which were mostly 343 fresh or palagonitized).

# 344 4.3 Important spectral ranges

Shapley values calculated for our ensemble predictions were aggregated to explore the contribution of each spectral range.

This result exploits the additive nature of Shapley values: values derived for bands in the VNIR, SWIR, MWIR and LWIR ranges (respectively) can be summed to quantify the aggregate effect of each spectral range on each model prediction (Fig. 7). The results suggest the VNIR-SWIR range contributes most to predictions of density, UCS, and E that are below the expected (average) prediction, while the LWIR range makes a substantial contribution for above-average predictions. The opposite can be seen for porosity, where VNIR-SWIR bands mostly drive above average predictions. This indicates that pattern suggests the models learn to associate SWIR-active alteration minerals with reduced UCS, E, and density (and associated increased porosity increase).

353 PerThe non-aggregated (per-band) Shapley values can also constrain the specific spectral features that, in combination, 354 contribute to each prediction. To reduce the influence of lithological effects, these per-band Shapley values were 355 ealeulated increase or decrease each prediction relative to the mean. These values are shown in Fig. 8, though only for models 356 trained only on the basaltic (Fig. 8a) and andesitic subsets (Fig. 8). The results highlight a sensitivity to spectral ranges 357 matching the expected mineralogical absorptions, though it is striking that the informative bands tend to occur on the 358 absorption "shoulders" rather than their centres (Fig. 8). 8c) subsets separately (to reduce the influence of lithological effects). The results are difficult to interpret specifically 360 because the predictions result from a complex balance between positive contributions from some bands (red) and negative 361 contributions (blue) from others. Strongly negative Shapley values are often associated with 1800, 1900, and 2200 nm bands, 362 which contain absorptions characteristic of hydrothermal alteration minerals (Table 1) for samples with low predicted E. 363 Higher predictions also appear driven by these same bands, presumably possibly due to an absence of absorption features in 364 these wavelengths for these samples. In the MWIR, features at ~3400 and between 4200 and 4900 nm appear important, with 365 several "doublets" (spectrally adjacent high and low Shapley values) indicating a sensitivity to absorption shape (asymmetry) 366 or position. The first of these bands (3400 nm) is likely related to v2HOH absorptions (though this absorption will have been 367 quiteheavily distorted by the hull correction applied during pre-processing). The latter bands (4200–4900) are interpreted to 368 relate to 2vSi-O absorptions from silicate minerals or 2vS-O absorptions from sulphates (Laukamp et al., 2021), though the 369 The last of these (4900) may also have been shifted by the hull correction. 370 The Shapley values are easier to interpret after averaging their absolute value across all samples, to broadly highlight 371 important spectral ranges. As mentioned also above, these ranges (Fig. 8b and Fig. 8d) match several expected mineralogical 372 absorptions but, interestingly, also suggest that the model tends to focus on absorption "shoulders" rather than their centres, 373 which we speculate could be due to a higher sensitivity of absorption shoulders to complex scattering effects. 374 Notably, many more VNIR, SWIR, and MWIR bands appear important for predictions made by the andesitic model than the 375 basaltic one, presumably due to the more complex mineralogy of these samples. Informative bands in the LWIR range 376 between 8500 and 11000 nm and also likely relate to vSiO absorptions, though the mixtures of silicate minerals and glassy 377 matrix make these difficult to interpret specifically (Laukamp et al., 2021; Leight et al., 2024; Williams and Ramsey, 2024). 378 Informative bands for the andesite model are lower wavelength (8500–9200 nm) than those for the basaltic model

#### 380 5 Discussion

381 Our five-fold cross validated ensemble predictions show that hyperspectral data can be used to explain ~80% of the variance 382 in density and porosity and 65–70% of the variance in strength (UCS) and Young's modulus (E), at least for the investigated 383 basaltic and andesitic volcanic lithologies. The rapid acquisition and imaging abilities of hyperspectral sensors could thus be 384 leveraged to better characterise complex volcanic rock masses, by extending laborious rock property measurements across

379 (8800–9800 nm), corroborating the change in silica polymerization between these sample sets.

385 large datasets from point spectrometers, hyperspectral core scanners and, potentially, outcrop hyperclouds (e.g., Thiele et al., 386 2024, 2022). The resulting thousands to millions of (ideally spatially continuous) property estimates would allow robust 387 characterisation of the variability in volcanic rock matrix properties and, if combined with digitally mapped fracture 388 information, provide some of the information needed to numerically predict larger-scale rock-mass properties (e.g., Cundall 389 et al., 2008).

391 Our predictions of density and porosity were remarkably accurate (5-fold CV R2 score of 0.81 and 0.84 respectively),

# 390 5.1 Predicting density and porosity

392 especially given the complex volcanic processes that influence these properties (vesiculation, pyroclastic processes, 393 alteration, and fracturing). Interestingly, linear methods such as LASSO and PLSR predicted density and porosity poorly 394 (Table 2), while the non-linear methods (MLP and SVR) achieved R2 scores >0.8. This suggests an inherently non-linear 395 relationship between reflectance, density, and porosity. The high accuracies of the non-linear models also indicate that they 396 are able to learn more than just the link between the hyperspectral data and mineralogy, as composition alone is expected to 397 be a poor predictor of porosity (Pola et al., 2012). We thus suggest that the hyperspectral data contain information on 398 porosity and density via the sensitivity of volume and surface scattering processes to pores at or near the sample's surface 399 (Fig. 1). As described by the Hapke model, such wavelength-dependent scattering effects are likely especially relevant for 400 longer wavelengths, supporting the Shapley values that show the LWIR data contributed significantly to many predictions 401 (Fig. 7). Larger vesicles that approach the 1 to 2 mm spatial resolution of the sensors could also influence the spectra, via the 402 cavity effect (Fig. 1), especially in the LWIR infrared range (where they are expected to reduce reflectivity and increase the 403 emissivity). 404 Our Shapley values highlight the important role of MWIR and LWIR bands, especially for high-density and low-porosity 405 samples (Fig. 7). It is also striking that the VNIR-SWIR and LWIR ranges tend to be in opposition (cancelling each other 406 out) for less extreme predictions (Fig. 7), emphasising the importance of the broad spectral range 407 (VNIR-SWIR-MWIR-LWIR) covered by the dataset. The special attention our machine learning models appear to be giving 408 to the shoulders of mineralogical absorption features (rather than their minima, which are typically related to composition) is 409 also noteworthy. We tentatively suggest that this highlights the sensitivity of our models to the shape and asymmetry of 410 absorption features, properties that are more significantly influenced by surface reflection and volume scattering processes 411 that likely give crucial information on surface roughness, grain size, and porosity.

#### 412 5.2 Predicting uniaxial compressive strength and Young's modulus

413 The lower, but still informative, predictive power of our models for UCS and E indicates a complex relationship between 414 spectral response, porosity, density, and alteration-related weakening (Heap et al., 2020a, or possibly strengthening in the 415 case of silicification; Heap et al., 2021a). These non-linear models can explain ~70% of the total variance, noting that the R2 416 scores are likely substantially reduced by a small number of outliers (Fig. 6). This result is consistent with the combined

- 417 models of Kereszturi et al. (2023), in which externally measured porosity and VNIR-SWIR information (characterising
- 418 alteration mineralogy) explained 80% of the variance in UCS. We suggest that externally measured porosity was needed by
- 419 Kereszturi et al. (2023) due the lack of LWIR information, which limited their ability to directly predict porosity from the
- 420 hyperspectral data (R2 = 0.4). Our dataset clearly did not have this limitation (Section 5.1), indirectly improving also our
- **421** predictions of UCS.
- 422 Theoretical links between reflectance spectra and grain size properties could further influence our machine learning models,
- 423 although we are unable to distinguish these effects from the previously discussed sensitivity to porosity. We also speculate
- 424 that it is likely the model is learning to distinguish glass-rich (and hence stiff and brittle) samples from more crystallised
- 425 ones, based on their distinctive LWIR expression (Williams and Ramsey, 2024). The sensitivity to glass could explain the
- 426 broad informative wavelength range indicated by the Shapley values in the LWIR (Fig. 8).
- 427 The remaining (unpredicted) variance in UCS and E could be attributed to micro-fractures, which will serve to reduce E and
- 428 UCS (Griffiths et al., 2017; Swanson et al., 2020; Takemura et al., 2003) with negligible spectral effect. Such fractures could,
- 429 for example, explain overpredicted outliers in Figs. 6 and 8. Micro-fractures are less likely to explain cases where our model
- 430 makes under-predictions however, including the notable outlier in Fig. 6c where the predicted UCS is ~250 MPa too low.

# 431 5.3 Hyperspectral quantification of hydrothermal alteration

- 432 VNIR-SWIR hyperspectral data are particularly useful for identifying hydrothermal alteration, discriminating between
- 433 different alteration types, and vectoring towards mineral deposits (e.g., Cudahy et al., 2008; Laukamp et al., 2021, 2011;
- 434 Portela et al., 2021). Argillic and advanced argillic alteration can be characterised based on the distinctive spectral signature
- 435 of sulphates, kaolinite, and other clay minerals (Fig. 4). This could be further refined by detailed investigation of the position
- 436 of these respective absorption features, to distinguish between e.g., kaolinite and dickite or illite and smectite (e.g.,
- 437 Kereszturi et al., 2020; Simpson and Rae, 2018).
- 438 Our results also show that the combined depth of v-OH and v+ $\delta$ H-O-H absorptions can be used as a broad but useful proxy
- 439 for hydrothermal alteration in non-weathered crystallised volcanic rocks, as these lithologies tend to be initially water poor.
- 440 That said, this index likely cannot identify hydrothermal alteration in tuff units, which can be hydrated during or shortly after
- 441 formation (e.g., palagonite). Our hydration index shows a weak correlation with physical and mechanical properties (Fig. 5),
- 442 with substantial unexplained variance that emphasises the important additional influence of microstructure (porosity,
- 443 grain-size, glass content, and micro-fractures).
- 444 <del>¶</del>

# 445 5.4 Applications and future directions

- 446 Unlike other commonly applied proxies for physical and mechanical rock properties (e.g., Schmidt hardness, field estimates
- 447 for porosity, etc.), hyperspectral data can be collected remotely using imaging techniques. This imaging capability unlocks
- 448 several intriguing possibilities.

449 Firstly, our machine learning models could be applied to hyperspectral imagery of hand-sample sized specimens acquired 450 during geotechnical fieldwork to create prior predictions of their physical and mechanical property variability. The locations 451 of extracted mechanical test cores could then be optimized to cover the range of expected variability, improving the 452 statistical representativity of the resulting data. Such an approach would provide an opportunity to independently validate our 453 model predictions, and provide training data for future refinements, while helping ensure statistically representative 454 characterisation of heterogeneous rock masses. 455 Secondly, imaging hyperspectral sensors can also be deployed on tripod, crewed, and uncrewed aircraft to remotely capture 456 ∼1 to 10 cm resolution data over large areas of exposed rock. This resolution is comparable to the scale of laboratory tests for 457 physical and mechanical properties, but with a large spatial extent that could enable detailed rock-mass characterisation, 458 through the integration of remotely estimated physical and mechanical property estimates, remotely mapped fracture 459 information (e.g., Dewez et al., 2016; Thiele et al., 2017), and numerical simulation techniques (e.g., Cundall et al., 2008; 460 Ivars et al., 2007). Further 461 Finally, we caution that further development and the acquisition of a larger, more diverse training database is undoubtedly 462 needed before our modelsthis approach can be confidently applied to such "outcrop" settings, due to the industrial 463 applications, especially for outcrop mapping. The lower-quality of hyperspectral data acquired outside of laboratory 464 conditions (where sub-optimal illumination and atmospheric scattering can be problematic) and the variety of weathering 465 processes that can influence outcrop surfaces, require approaches that are robust and carefully validated. However, the

466 required sensors and acquisition techniques already exist, suggesting cm-scale mapping of outcrop physical and mechanical

467 properties is achievable, with appropriate site-specific calibration and validation, achievable.

#### 468 6 Conclusions

479

469 Our machine learning models demonstrate that hyperspectral data can be used as a proxy for the physical and mechanical 470 properties in the sampled andesitic and basaltic volcanic rocks, with cross validated R2 scores of 0.7 to 0.8. Physical 471 properties, mechanical behaviour, and reflection spectra are influenced by a complex combination of primary and secondary 472 (alteration or weathering) mineralogy, glass content, porosity, grain size, and surface roughness. Disentangling the influence 473 of these properties on spectral reflectance (for complex mixtures; i.e. rocks) remains challenging but our findings 474 demonstrated that machine learning techniques can be used to find informative relationships between spectral and physical 475 and mechanical properties. Further work is required to assess how robust these predictions are, and if they can be generalised 476 or are best applied after site-specific training. We are confident that our results (and other recent work by e.g., Bakun-Mazor 477 et al., 2024; Kereszturi et al., 2023) underpin how hyperspectral data can serve as informative and easy-to-acquire proxy for 478 physical and mechanical properties of volcanic rocks.

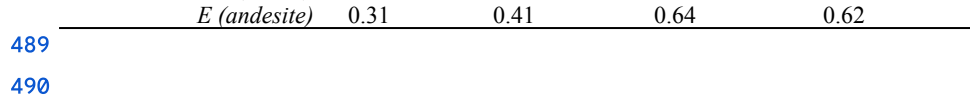
480 Table 1: Spectral indices used to spectrally characterize our samples. Absorption features are classified according to the notation 481 of Laukamp et al., (2021), denoting stretching-related absorptions with v and bending-related absorptions with v and were 482 quantified by fitting an asymmetric gaussian to the specified spectral range and recording its amplitude as a measure of 483 absorption depth. This fitting was conducted using hylite (Thiele et al., 2021), and included a hull correction step to remove 484 spectral features broader than the target range.

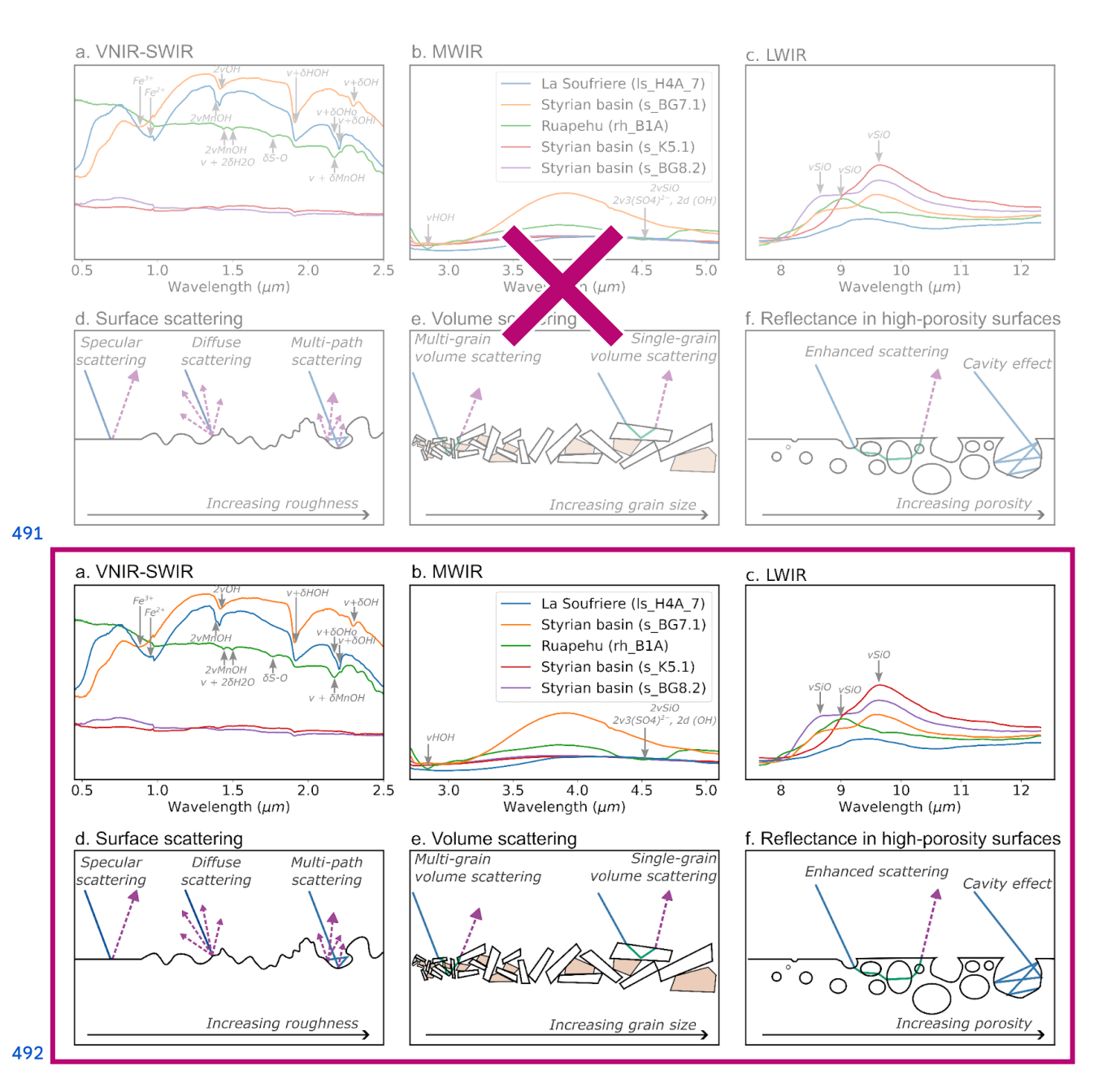
Short name	Target	Spectral range (nm)	Indicator for		
$\rm H_2O$	$vOH+\delta H_2O$	1800–2120	Molecular water in e.g., clay minerals.		
ОН	vOH	1350–1600	1350–1600 Hydroxyl groups in clay minerals and hydroxylated sulfates (kaolinite, alunite, illite, etc).		
Al-OH	$\nu + \delta(Al)$ -OH	2150–2240	Hydroxyl groups in Al-rich phyllosilicate minerals including illite, smectite, kaolinite, etc.		
Mg-OH	$\nu + \delta(Mg)OH$	2280–2330	Hydroxyl groups in Mg-bearing phyllosilicate, like Mg-rich smectites (e.g., hectorite).		
$\mathrm{SO}_4$	δSO	1700–1800	Indicator for the presence of sulfate-bearing minerals, including gypsum and alunite.		
Silica	vSiO	4400–4600 Indicator for quartz or amorphous silica via second overtone SiO absorption. This was u (rather than the LWIR feature) to avoid inte with plagioclase.			
Kaolinite	$v + \delta M2OHo$	2100–2200	Depth of the $v + \delta(Al)$ -OH related doublet typical of kaolinite group minerals. Note that the hull correction applied prior to fitting removes the influence of the deeper absorption at 2200 nm.		

486 Table 2: Five-fold cross validated R2 scores for the machine learning approaches trained and tested on: (1) basaltic (MFI < 0.4), (2) 487 andesitic (MFI > 0.4), and (3) combined subsets. The best R2 scores for each property are indicated in bold. The ensemble models 488 were constructed by combining the best-performing SVR and MLP models.

	Lasso	PLSR	SVR	MLP (uni)	MLP (multi)	Ensemble
Density	0.39	0.51	0.76	0.82	0.85	0.84
Density (basalt)	0.5	0.47	0.77	0.75	0.83	0.78
Density (andesite)	0.32	0.47	0.79	0.85	0.83	0.84
Porosity	0.33	0.48	0.74	0.79	0.81	0.81
Porosity (basalt)	0.39	0.49	0.77	0.73	0.81	0.76
Porosity (andesite)	0.31	0.49	0.74	0.80	0.77	0.80
UCS	0.21	0.18	0.59	0.69	0.66	0.67
UCS (basalt)	0.56	<0	0.76	0.76	0.75	0.75
UCS (andesité)	0.1	<0	0.57	0.67	0.67	0.66
E	0.30	0.36	0.65	0.67	0.67	0.70







493 Figure. 1: Mineralogical and physical controls on hyperspectral reflectance spectra. Examples of absorption features caused by 494 minerals commonly found in volcanic rocks are shown for the VNIR-SWIR (a), MWIR (b) and LWIR (c) ranges, as described in

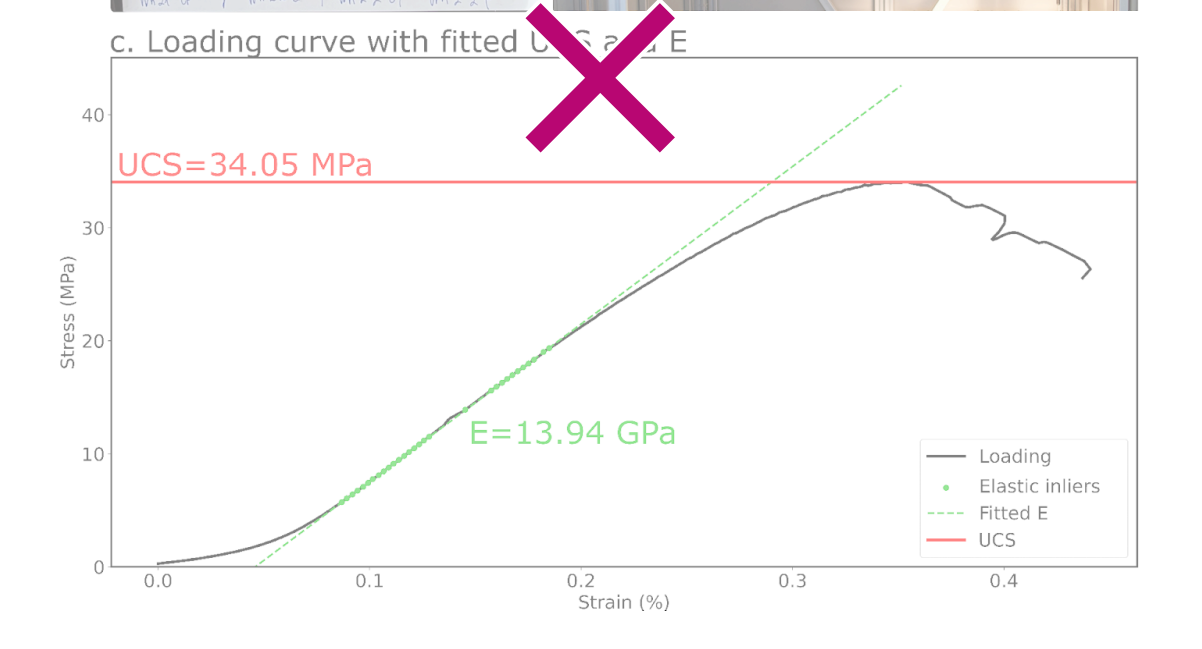
- 495 depth by Laukamp et al., (2021). Typical surface (d) and volume scattering (e) interactions are shown, highlighting the effect of
- 496 increasing surface roughness and grain size. An example of how these processes operate simultaneously, and are both strongly
- 497 influenced by porosity, is shown in (f). Note that these are all wavelength dependent, especially where the wavelength of light
- 498 approaches the scale of variation.

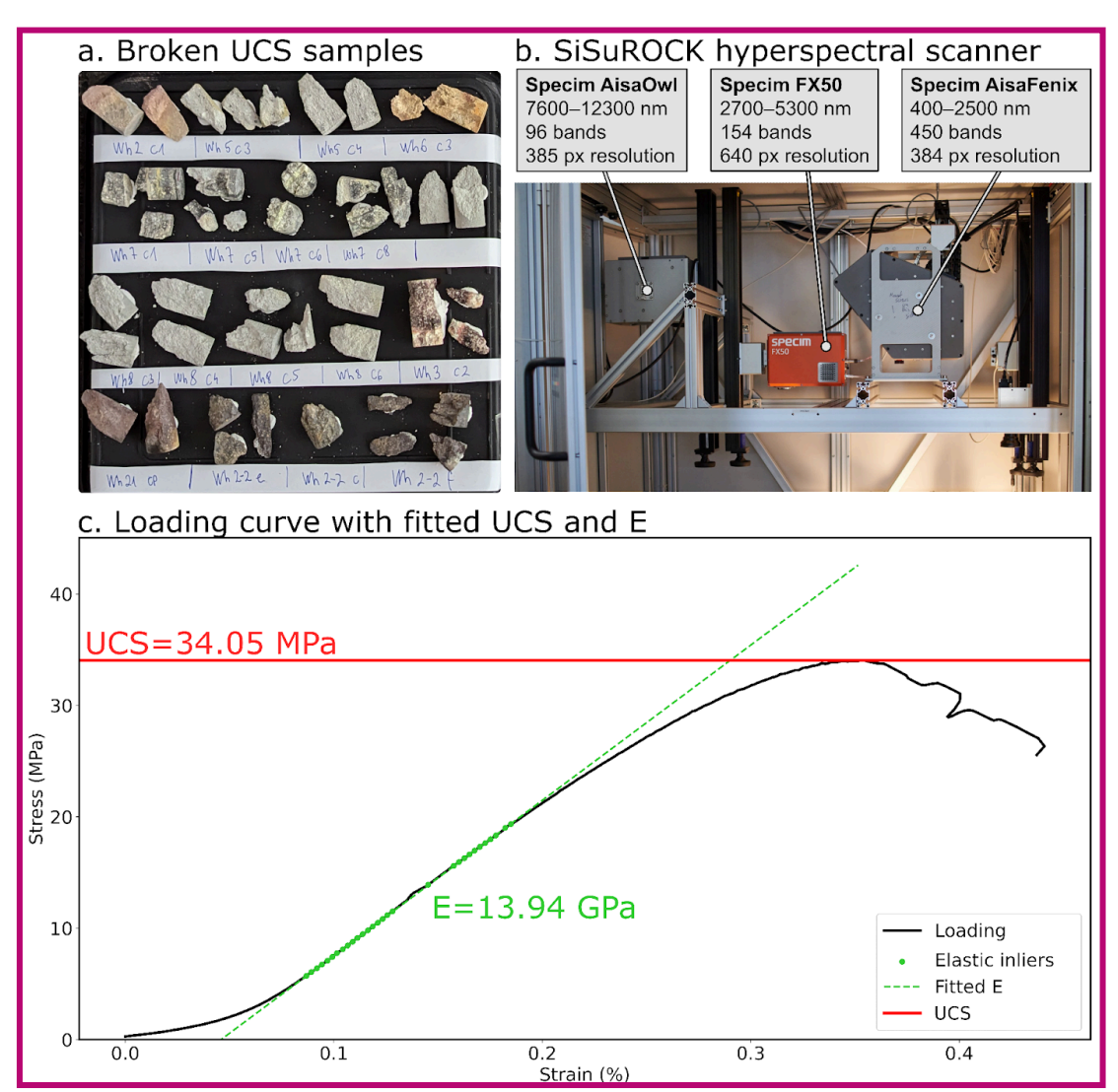
a. Broken UCS samples

b. SiSuROCK hyperspectral scanner

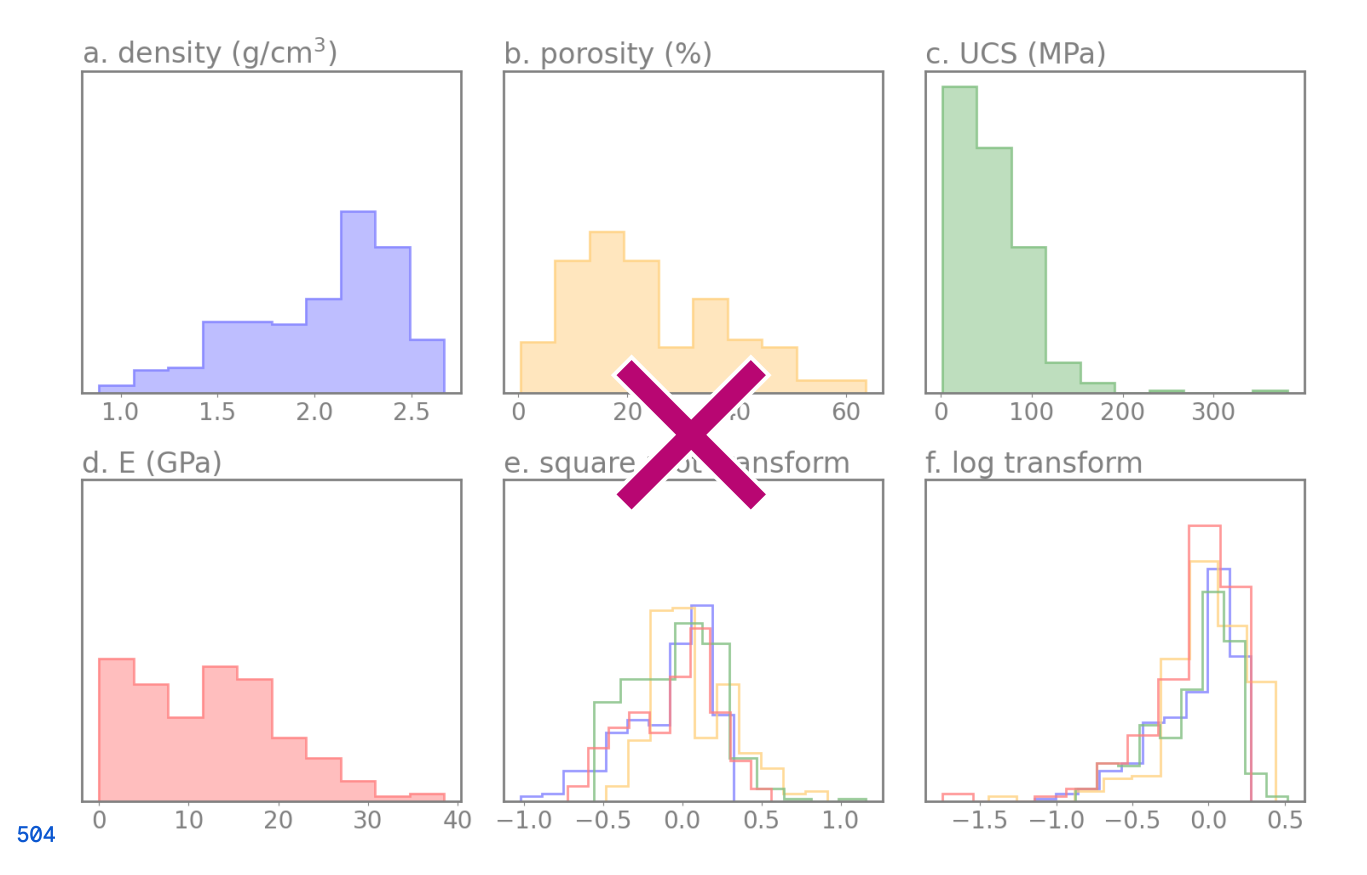
Specim AisaOwl 7600—12300 nm 96 bands 385 px resolution

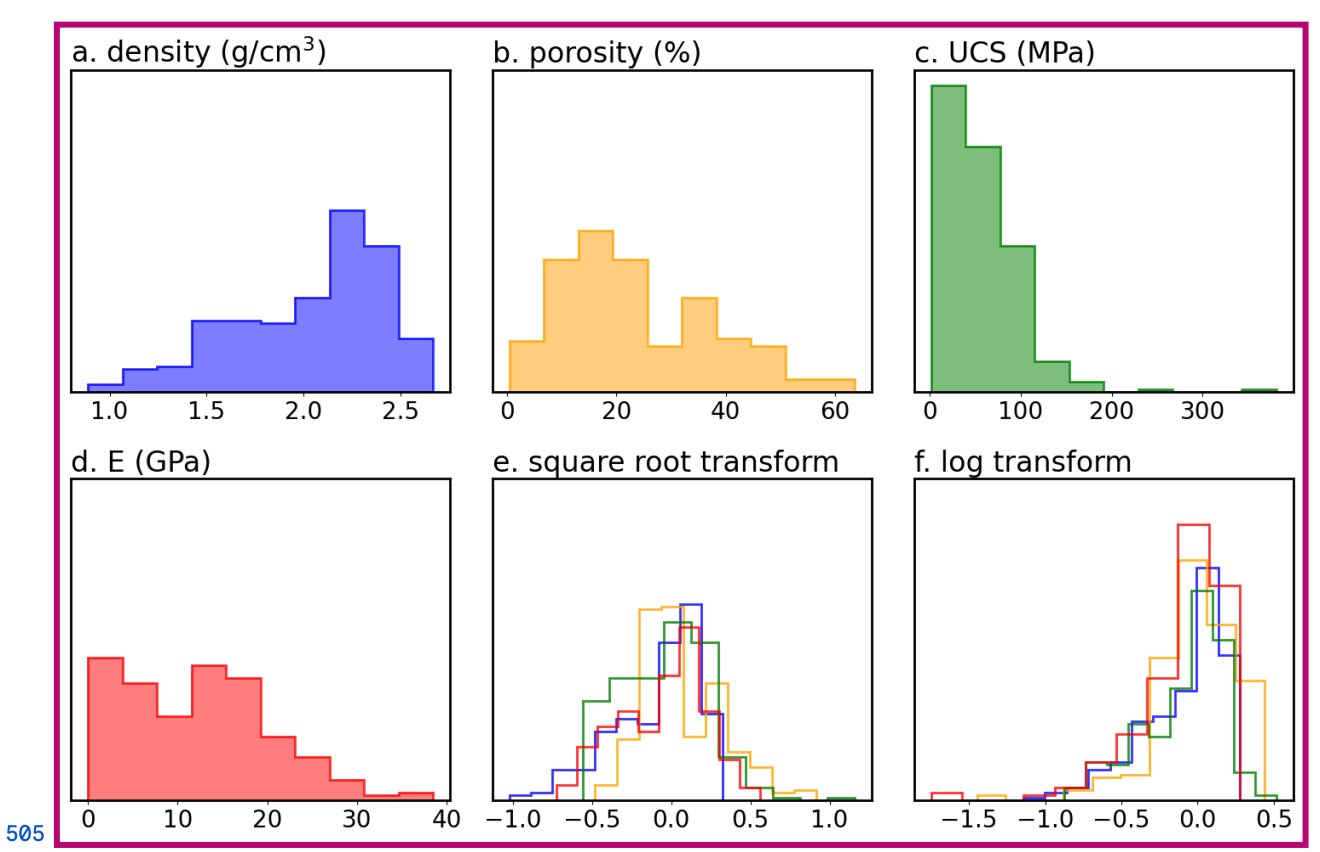
White of White



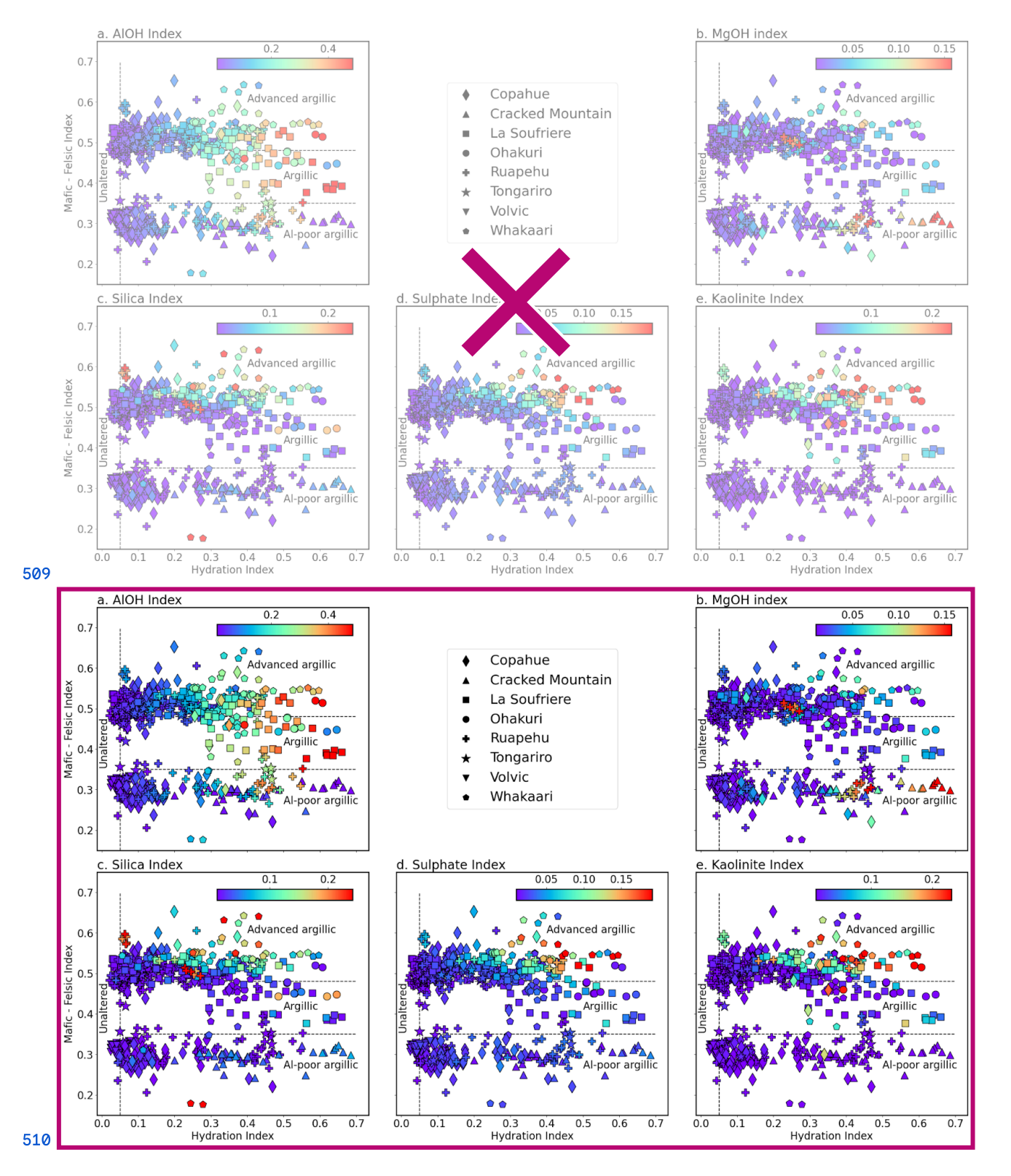


501 Figure. 2: Post-failure uniaxial compressive strength (UCS) test cores (a) prior to scanning in a SiSuROCK hyperspectral drillcore 502 scanner (b). UCS and Young's modulus (E) were extracted from the corresponding stress-strain curves (c) using an automated 503 RANSAC-based procedure, for direct comparison with the (averaged) sample spectra.

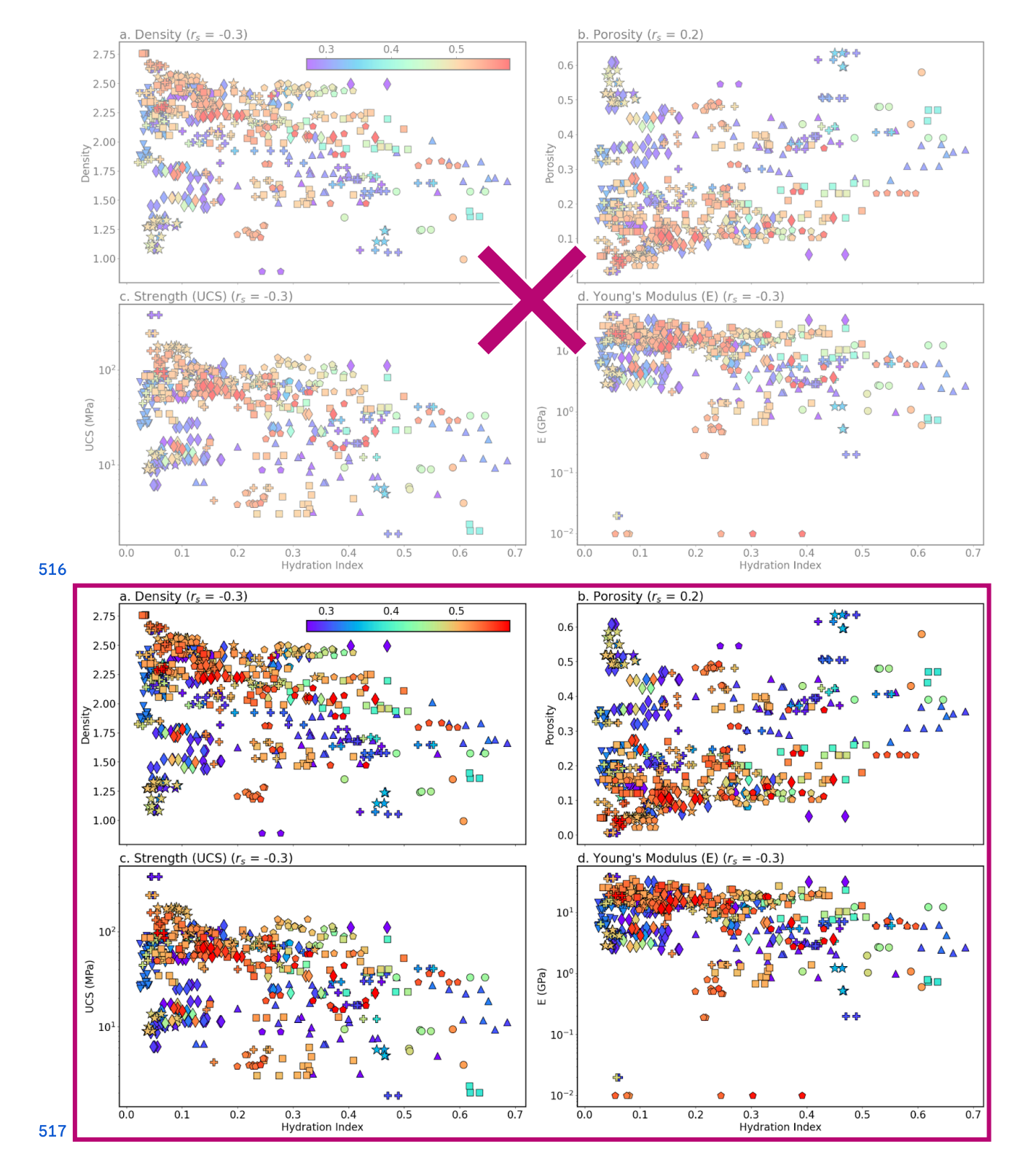




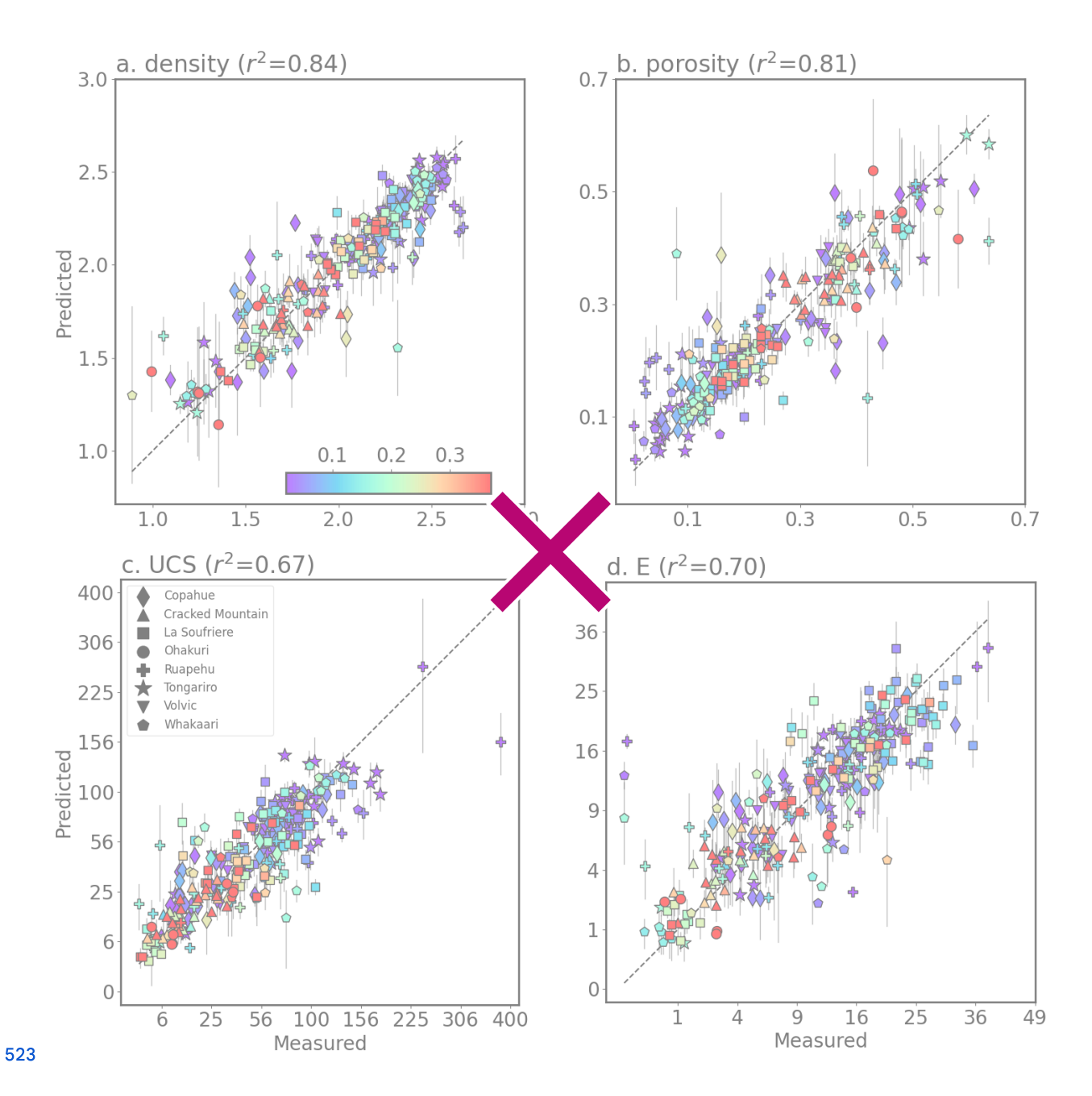
506 Figure. 3: Distributions of the training data before (a-d) and after square root (e) and log (f) transformation. Note that 507 transformed data was normalised to have a median of 0 and 2nd to 98th percentile range of 1. The square root transform (e) 508 resulted in approximately normal distributions.

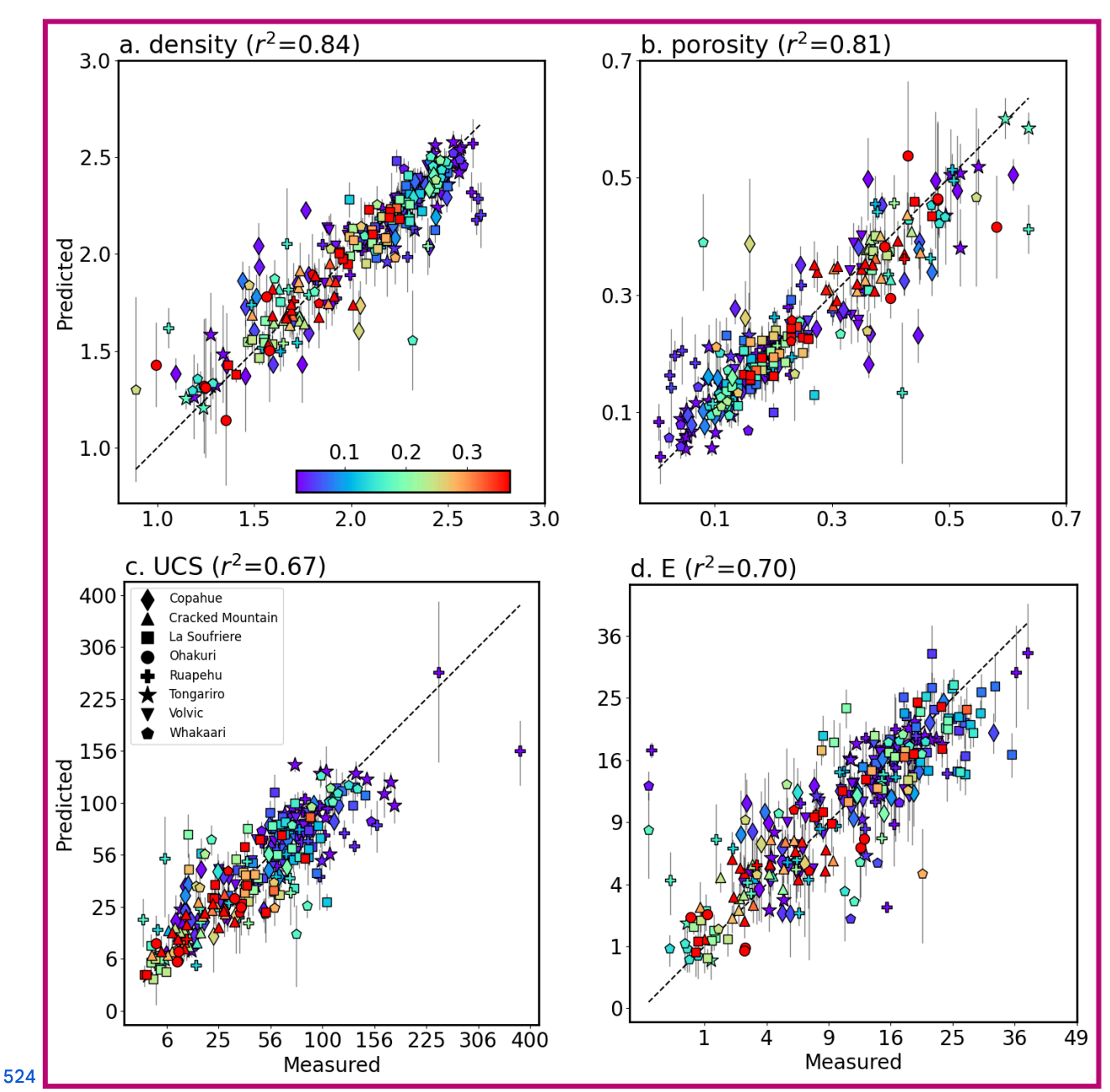


- 511 Figure. 4: Measured hydration index (x-axis) and Mafic-Felsic Index (MFI; y-axis), coloured by hyperspectral indices for Al-OH
- 512 bearing phyllosilicates (a), Mg-OH bearing phyllosilicates such as hectorite (b), quartz (c), sulfate (d), and kaolinite (e). The two
- 513 main clusters indicate the broadly basaltic (lower) or andesitic (upper) composition of the samples, while hydrothermal alteration
- 514 (and/or surface weathering) results in significant scatter along the x-axis. Distinctive Al-OH and Mg-OH (clay) rich zones indicate
- 515 argillic alteration, while samples with elevated sulfate and kaolinite indices were likely subject to advanced argillic alteration.

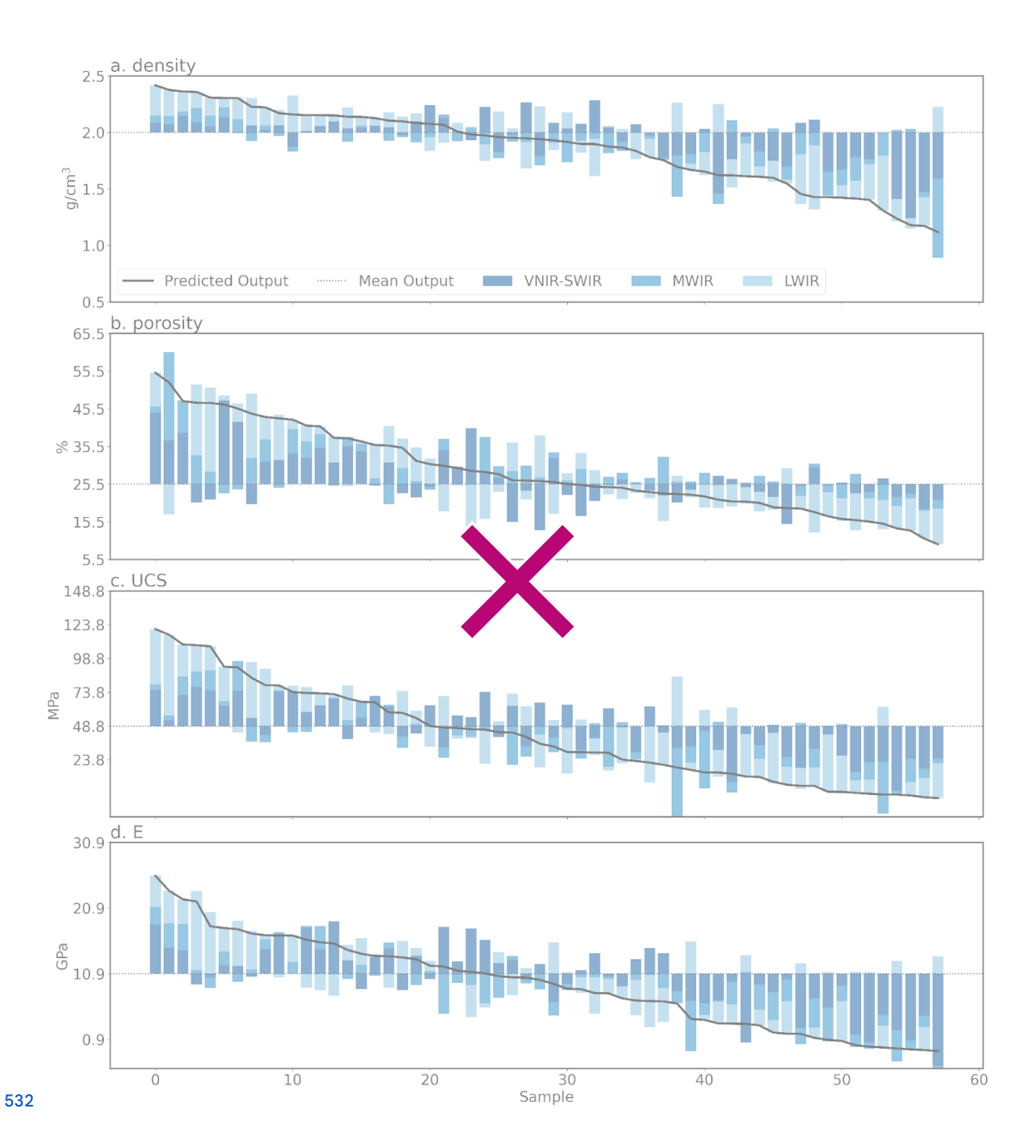


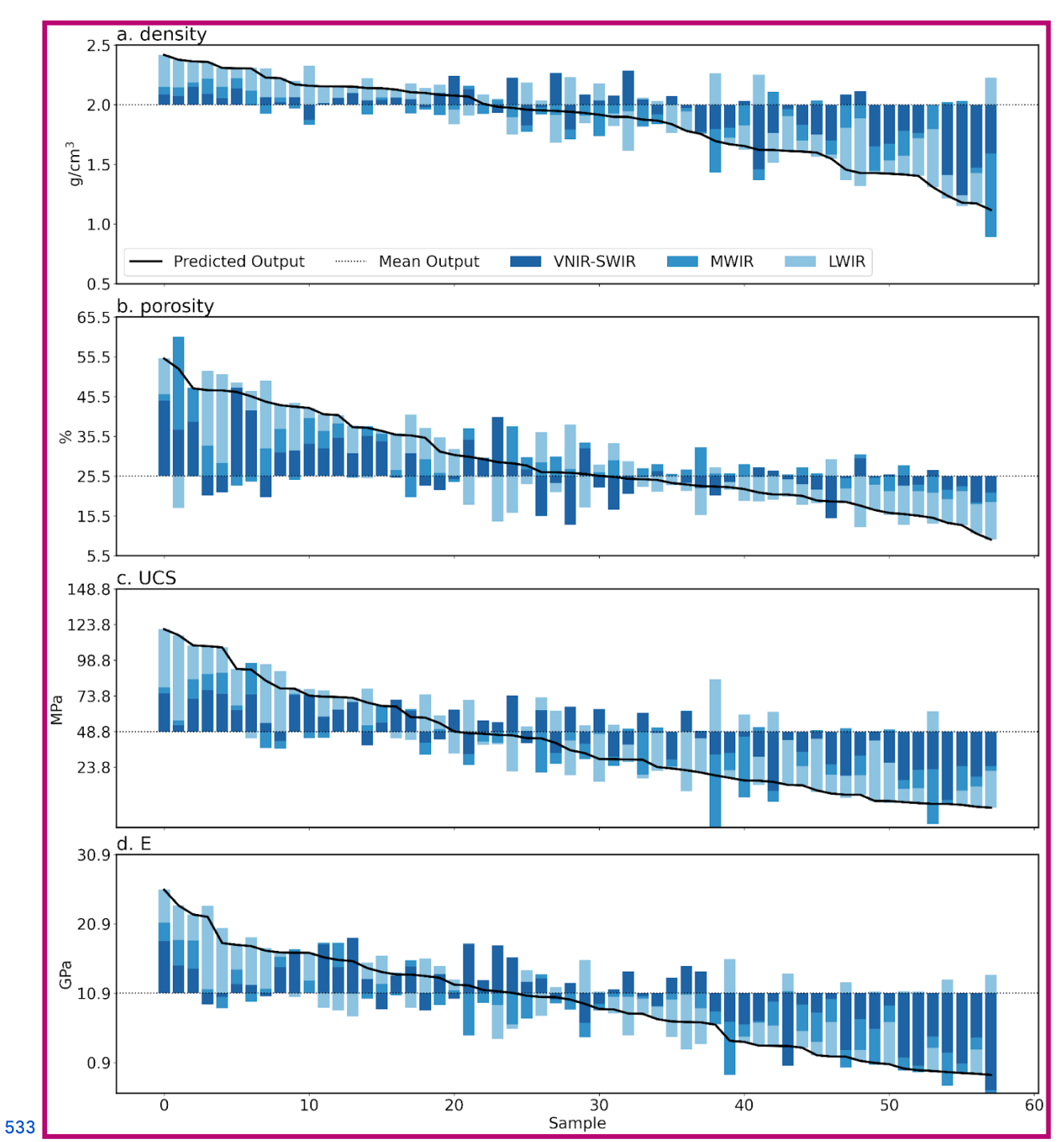
- 518 Figure. 5: Biplots of our hydration index and density (a), porosity (b), uniaxial compressive strength (UCS) (c) and Young's
- 519 modulus (E) (d). These indicate that increasing hydration due to hydrothermal alteration and/or weathering tends to decrease
- 520 density, UCS and E and slightly increase porosity. These trends are (unsurprisingly) quite weak, with Spearman rank correlation
- 521 coefficients of 0.2-0.3. Colours indicate each sample's MFI, such that basalts are blue and andesites are red. Please refer to the
- 522 legend of Fig. 3 for the symbols indicating each volcano.





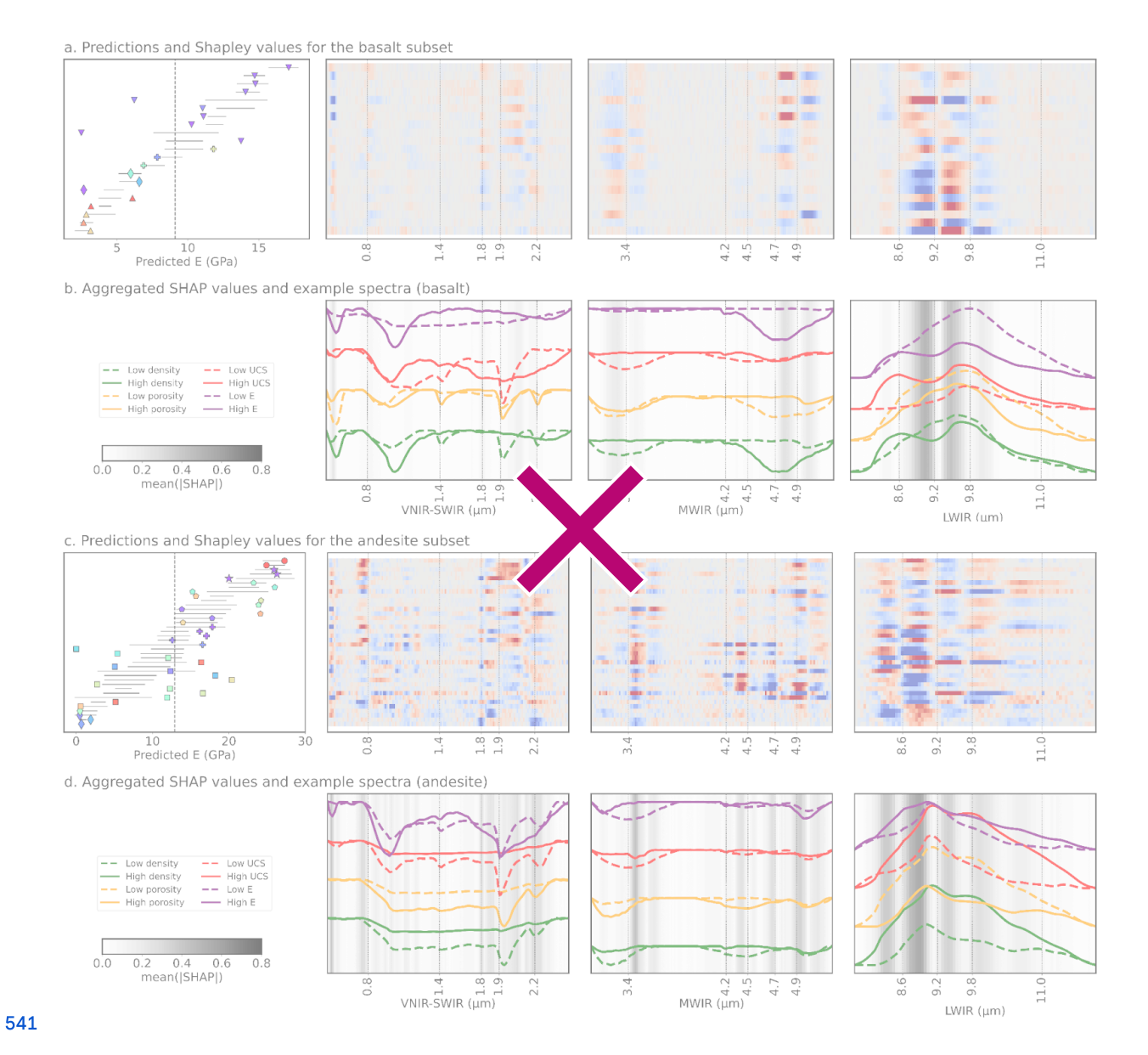
525 Figure. 6: Five-fold cross validation predictions (test-fold predictions for each of the five models) for density (a), porosity (b), 526 uniaxial compressive strength (UCS) (c) and Young's modulus (E) (d) derived using our ensemble of SVM and multilayer 527 perceptron models. The consistency of the ensemble predictions, quantified as the standard deviation of model predictions, are 528 shown as  $2\sigma$  error bars. The majority of the predictions are thus within error of the measured values, although there are also 529 several notable outliers. Symbols denote the different volcanoes included in the dataset, and colours reflect the hydration index 530 (Fig. 3). Note that the x- and y-axes in (c) and (d) use a square-root scale to better visualise data clustered around lower values of 531 UCS and E.





534 Figure. 7: Shapley values summed for each spectral range (VNIR-SWIR, MWIR, and LWIR) from the joint model (trained on 535 both basalt and andesite) ensemble, indicating the cumulative contribution of each spectral range to predicted density (a), porosity 536 (b), uniaxial compressive strength (UCS) (c) and Young's modulus (E) (d). Values for each property are sorted from high to low 537 predicted value along the x-axis. Higher predictions relative to the mean prediction (dotted line) for density, UCS, and E appear 538 largely driven by LWIR features, while lower values are associated with strong negative contributions from the VNIR-SWIR

539 range. These VNIR-SWIR bands push the predicted value down, and likely indicate the influence of SWIR active hydrated 540 alteration minerals.



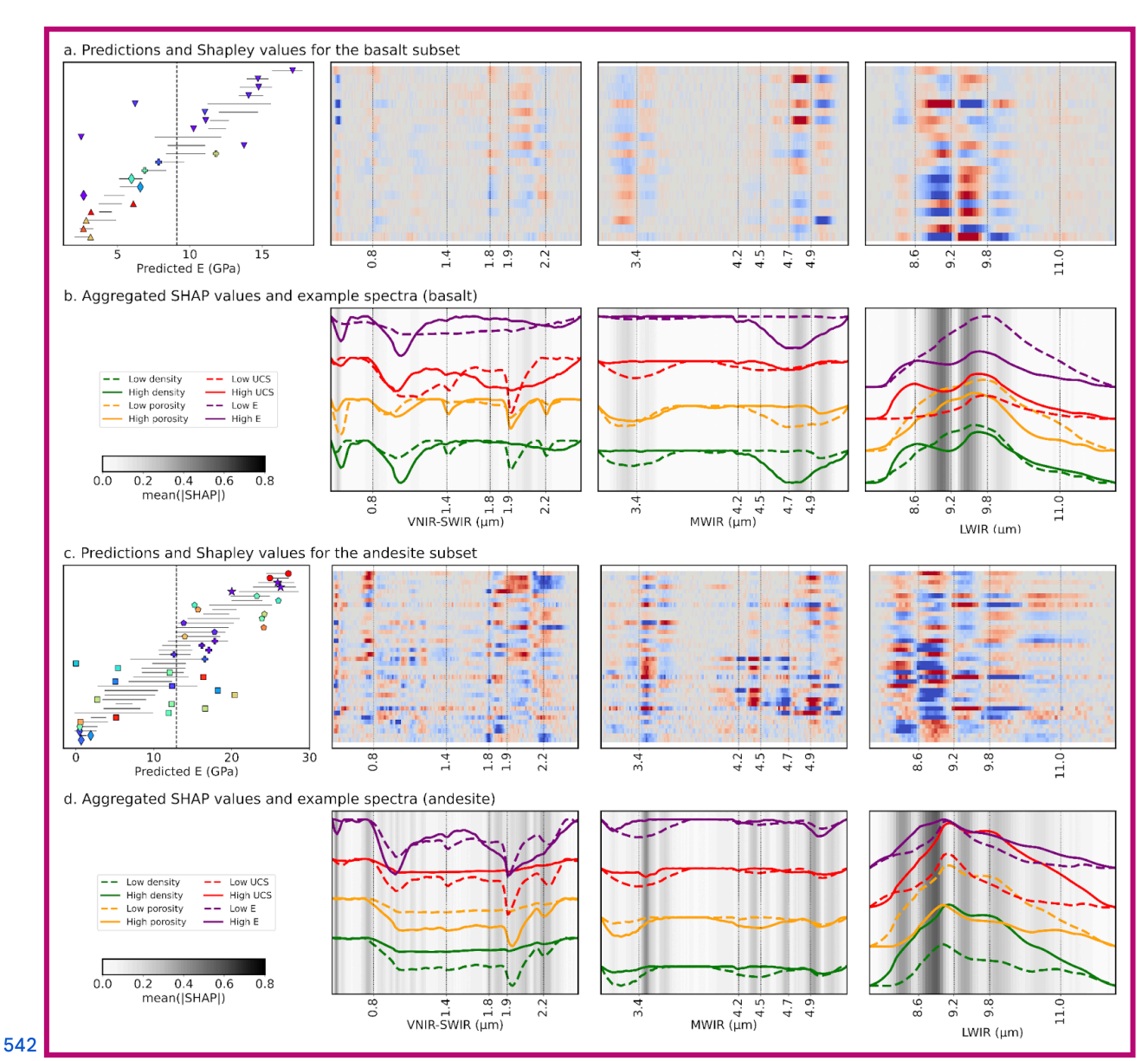


Figure. 8: Shapley values for our predictions of Young's modulus (E) in the basaltic (a, b) and andesitic (c, d) subsets. These were calculated using the ensemble models trained specifically on each subset (to remove aspects of the joint model focused on lithological distinction). Symbols in the left column indicate the measured property values from each volcano (cf. Fig. 3), while the black solid lines show the  $(2\sigma)$  range of values predicted by the ensemble. Deviations of model predictions from the mean (black dashed line) are the sum of the Shapley values along each row, such that blue values indicate bands that decreased the prediction, while red values indicate bands that increased it. Mean absolute SHAP values (b, d), summarising the sensitivity of the model to specific bands are also shown, with spectra from samples with high (solid) and low (dashed) property values for reference. These Shapley values highlight the correspondence of informative bands and inflection points ("shoulders") in the spectra. Shapley value plots for the other mechanical properties can be found in the supplementary information.

#### 552 Acknowledgements

553 ST and AK were supported by funding from the European Union's Horizon Europe research and innovation programme 554 under grant agreement no 101058483 and from UK Research and Innovation. GK was supported by the Rutherford 555 Discovery Fellowship of the Royal Society of New Zealand - Te Aparangi ("Caught in action - volcano surveillance with 556 hyperspectral remote sensing"; RDF-MAU2003). MH was supported by ANR grant MYGALE ("Modelling the phYsical 557 and chemical Gradients of hydrothermal ALteration for warning systems of flank collapse at Explosive volcanoes"; 558 ANR-21-CE49-0010) and a European Research Council Synergy Grant (ERC-ROTTnROCK-101118491). MH also 559 acknowledges support from the Institut Universitaire de France (IUF). MRC and MT were supported by the TelluS Program 560 of INSU-CNRS ("Edifice structure and rock strength assessment of Copahue volcano (Argentina/Chile): the role of 561 hyperACidic hydrothermal alteration in VolCano stability (AC/VC))". The hyperspectral sensors used for this study were 562 acquired through funding from the Helmholtz Institute Freiberg for Resource Technology, European Regional Development 563 Fund and the Land of Saxony

## **564 References**

- 565 Arens, F., Coco, A., Gottsmann, J., Hickey, J., Kilgour, G., 2022. Multiphysics Modeling of Volcanic Unrest at Mt. Ruapehu
- 566 (New Zealand). Geochem. Geophys. Geosystems 23, e2022GC010572. https://doi.org/10.1029/2022GC010572
- 567 Aubry, T.J., Farquharson, J.I., Rowell, C.R., Watt, S.F.L., Pinel, V., Beckett, F., Fasullo, J., Hopcroft, P.O., Pyle, D.M.,
- 568 Schmidt, A., Sykes, J.S., 2022. Impact of climate change on volcanic processes: current understanding and future
- challenges. Bull. Volcanol. 84, 58. https://doi.org/10.1007/s00445-022-01562-8
- 570 Bakun-Mazor, D., Ben-Ari, Y., Marco, S., Ben-Dor, E., 2024. Predicting Mechanical Properties of Carbonate Rocks Using
- 571 Spectroscopy Across 0.4–12 μm. Rock Mech. Rock Eng. 57, 8951–8968. https://doi.org/10.1007/s00603-024-04035-w
- 572 Chandrasekhar, S. (Subrahmanyan), 1960. Radiative transfer. New York: Dover Publications.
- 573 Cudahy, T., Jones, M., Thomas, M., Laukamp, C., Caccetta, M., Hewson, R., Rodger, A., Verrall, M., 2008. Next generation
- mineral mapping: Queensland airborne HyMap and satellite ASTER surveys 2006–2008. Perth Publicly Available Rep.
- **575** P2007364 152.
- 576 Cundall, P.A., Pierce, M.E., Mas Ivars, D., 2008. Quantifying the size effect of rock mass strength, in: SHIRMS 2008:
- 577 Proceedings of the First Southern Hemisphere International Rock Mechanics Symposium. Australian Centre for
- 578 Geomechanics, pp. 3–15.
- 579 del Potro, R., Hürlimann, M., 2009. A Comparison of Different Indirect Techniques to Evaluate Volcanic Intact Rock
- 580 Strength. Rock Mech. Rock Eng. 42, 931–938. https://doi.org/10.1007/s00603-008-0001-5
- 581 Dewez, T.J.B., Girardeau-Montaut, D., Allanic, C., Rohmer, J., 2016. Facets: a cloudcompare plugin to extract geological
- planes from unstructured 3D point clouds. ISPRS Int. Arch. Photogramm. Remote Sens. Spat. Inf. Sci. XLI-B5, 799.
- 583 https://doi.org/10.5194/isprsarchives-xli-b5-799-2016

- 584 Dincer, I., Acar, A., Cobanoğlu, I., Uras, Y., 2004. Correlation between Schmidt hardness, uniaxial compressive strength and
- 585 Young's modulus for andesites, basalts and tuffs, Bull, Eng. Geol. Environ, 63, 141–148.
- 586 https://doi.org/10.1007/s10064-004-0230-0
- 587 Farquharson, J., Heap, M.J., Varley, N.R., Baud, P., Reuschlé, T., 2015. Permeability and porosity relationships of
- edifice-forming andesites: A combined field and laboratory study. J. Volcanol. Geotherm. Res. 297, 52–68.
- 589 https://doi.org/10.1016/j.jvolgeores.2015.03.016
- 590 Foster, S., Chilton, J., Nijsten, G.-J., Richts, A., 2013. Groundwater—a global focus on the 'local resource.' Curr. Opin.
- 591 Environ. Sustain., Aquatic and marine systems 5, 685–695. https://doi.org/10.1016/j.cosust.2013.10.010
- 592 Franzosi, F., Crippa, C., Derron, M.-H., Jaboyedoff, M., Agliardi, F., 2023. Slope-Scale Remote Mapping of Rock Mass
- Fracturing by Modeling Cooling Trends Derived from Infrared Thermography. Remote Sens. 15, 4525.
- 594 https://doi.org/10.3390/rs15184525
- 595 Griffiths, L., Heap, M.J., Baud, P., Schmittbuhl, J., 2017. Quantification of microcrack characteristics and implications for
- 596 stiffness and strength of granite. Int. J. Rock Mech. Min. Sci. 100, 138–150. https://doi.org/10.1016/j.ijrmms.2017.10.013
- 597 Hapke, B., 2012. Theory of Reflectance and Emittance Spectroscopy. Cambridge University Press.
- 598 Hapke, B., 2008. Bidirectional reflectance spectroscopy: 6. Effects of porosity. Icarus 195, 918–926.
- 599 https://doi.org/10.1016/j.icarus.2008.01.003
- 600 Hapke, B., 2002. Bidirectional Reflectance Spectroscopy: 5. The Coherent Backscatter Opposition Effect and Anisotropic
- 601 Scattering. Icarus 157, 523–534. https://doi.org/10.1006/icar.2002.6853
- 602 Hapke, B., 1993. Theory of Reflectance and Emittance Spectroscopy, Topics in Remote Sensing. Cambridge University
- 603 Press, Cambridge. https://doi.org/10.1017/CBO9780511524998
- 604 Hapke, B., 1986. Bidirectional reflectance spectroscopy: 4. The extinction coefficient and the opposition effect. Icarus 67,
- 605 264–280. https://doi.org/10.1016/0019-1035(86)90108-9
- 606 Hapke, B., 1984. Bidirectional reflectance spectroscopy: 3. Correction for macroscopic roughness. Icarus 59, 41–59.
- 607 https://doi.org/10.1016/0019-1035(84)90054-X
- 608 Hapke, B., 1981. Bidirectional reflectance spectroscopy: 1. Theory. J. Geophys. Res. Solid Earth 86, 3039–3054.
- 609 https://doi.org/10.1029/JB086iB04p03039
- 610 Hardgrove, C.J., Rogers, A.D., Glotch, T.D., Arnold, J.A., 2016. Thermal emission spectroscopy of microcrystalline
- sedimentary phases: Effects of natural surface roughness on spectral feature shape. J. Geophys. Res. Planets 121,
- 612 542–555. https://doi.org/10.1002/2015JE004919
- 613 Harnett, C.E., Heap, M.J., 2021. Mechanical and topographic factors influencing lava dome growth and collapse. J.
- 614 Volcanol. Geotherm. Res. 420, 107398. https://doi.org/10.1016/j.jvolgeores.2021.107398
- 615 Harnett, C.E., Kendrick, J.E., Lamur, A., Thomas, M.E., Stinton, A., Wallace, P.A., Utley, J.E.P., Murphy, W., Neuberg, J.,
- 616 Lavallée, Y., 2019. Evolution of Mechanical Properties of Lava Dome Rocks Across the 1995–2010 Eruption of
- 617 Soufrière Hills Volcano, Montserrat. Front. Earth Sci. 7. https://doi.org/10.3389/feart.2019.00007

- 618 Heap, M.J., Baumann, T., Gilg, H.A., Kolzenburg, S., Ryan, A.G., Villeneuve, M., Russell, J.K., Kennedy, L.A.,
- 619 Rosas-Carbajal, M., Clynne, M.A., 2021a. Hydrothermal alteration can result in pore pressurization and volcano
- 620 instability. Geology 49, 1348–1352. https://doi.org/10.1130/G49063.1
- 621 Heap, M.J., Baumann, T.S., Rosas-Carbajal, M., Komorowski, J.-C., Gilg, H.A., Villeneuve, M., Moretti, R., Baud, P.,
- 622 Carbillet, L., Harnett, C., Reuschlé, T., 2021b. Alteration-Induced Volcano Instability at La Soufrière de Guadeloupe
- 623 (Eastern Caribbean). J. Geophys. Res. Solid Earth 126, e2021JB022514. https://doi.org/10.1029/2021JB022514
- 624 Heap, M.J., Gravley, D.M., Kennedy, B.M., Gilg, H.A., Bertolett, E., Barker, S.L.L., 2020a. Quantifying the role of
- 625 hydrothermal alteration in creating geothermal and epithermal mineral resources: The Ohakuri ignimbrite (Taupō
- 626 Volcanic Zone, New Zealand). J. Volcanol. Geotherm. Res. 390, 106703.
- 627 https://doi.org/10.1016/j.jvolgeores.2019.106703
- 628 Heap, M.J., Troll, V.R., Harris, C., Gilg, H.A., Moretti, R., Rosas-Carbajal, M., Komorowski, J.-C., Baud, P., 2022.
- Whole-rock oxygen isotope ratios as a proxy for the strength and stiffness of hydrothermally altered volcanic rocks. Bull.
- 630 Volcanol. 84, 74. https://doi.org/10.1007/s00445-022-01588-y
- 631 Heap, M.J., Villeneuve, M., Albino, F., Farquharson, J.I., Brothelande, E., Amelung, F., Got, J.-L., Baud, P., 2020b. Towards
- more realistic values of elastic moduli for volcano modelling. J. Volcanol. Geotherm. Res. 390, 106684.
- 633 https://doi.org/10.1016/j.jvolgeores.2019.106684
- 634 Heap, M.J., Violay, M.E.S., 2021. The mechanical behaviour and failure modes of volcanic rocks: a review. Bull. Volcanol.
- 635 83, 33. https://doi.org/10.1007/s00445-021-01447-2
- 636 Hickey, J., Pascal, K., Head, M., Gottsmann, J., Fournier, N., Hreinsdottir, S., Syers, R., 2022. Magma pressurization
- sustains ongoing eruptive episode at dome-building Soufrière Hills volcano, Montserrat. Geology 50, 1261–1265.
- 638 https://doi.org/10.1130/G50239.1
- 639 Hoek, E., Diederichs, M.S., 2006. Empirical estimation of rock mass modulus. Int. J. Rock Mech. Min. Sci. 43, 203–215.
- 640 Huang, J., Liu, S., Liu, W., Zhang, C., Li, S., Yu, M., Wu, L., 2021. Experimental Study on the Thermal Infrared Spectral
- Variation of Fractured Rock. Remote Sens. 13, 1191. https://doi.org/10.3390/rs13061191
- 642 Hunt, G.R., Vincent, R.K., 1968. The behavior of spectral features in the infrared emission from particulate surfaces of
- various grain sizes. J. Geophys. Res. 1896-1977 73, 6039–6046. https://doi.org/10.1029/JB073i018p06039
- 644 Ivars, D.M., Deisman, N., Pierce, M., Fairhurst, C., 2007. The synthetic rock mass approach-a step forward in the
- characterization of jointed rock masses, in: 11th ISRM Congress. OnePetro.
- 646 Kamath, A.V., Thiele, S.T., Kirsch, M., Gloaguen, R., 2025. Multiphysics property prediction from hyperspectral drill core
- data. Solid Earth, 16(4/5), 351-365. https://doi.org/10.5194/se-16-351-2025
- 648 Kereszturi, G., Heap, M., Schaefer, L.N., Darmawan, H., Deegan, F.M., Kennedy, B., Komorowski, J.-C., Mead, S.,
- Rosas-Carbajal, M., Ryan, A., Troll, V.R., Villeneuve, M., Walter, T.R., 2023. Porosity, strength, and alteration Towards
- a new volcano stability assessment tool using VNIR-SWIR reflectance spectroscopy. Earth Planet. Sci. Lett. 602, 117929.
- 651 https://doi.org/10.1016/j.epsl.2022.117929

- 652 Kereszturi, G., Schaefer, L.N., Miller, C., Mead, S., 2020. Hydrothermal Alteration on Composite Volcanoes: Mineralogy,
- 653 Hyperspectral Imaging, and Aeromagnetic Study of Mt Ruapehu, New Zealand. Geochem. Geophys. Geosystems 21,
- e2020GC009270. https://doi.org/10.1029/2020GC009270
- 655 Kidd, M., Kereszturi, G., Kennedy, B., Heap, M., Procter, J., 2025. Linking hydrothermal alteration to rock mechanics:
- comparative analysis of andesitic volcanoes in Aotearoa New Zealand.
- 657 Kirkland, L.E., Herr, K.C., Adams, P.M., 2003. Infrared stealthy surfaces: Why TES and THEMIS may miss some
- substantial mineral deposits on Mars and implications for remote sensing of planetary surfaces. J. Geophys. Res. Planets
- 659 108. https://doi.org/10.1029/2003JE002105
- 660 Kirkland, L.E., Herr, K.C., Salisbury, J.W., 2001. Thermal infrared spectral band detection limits for unidentified surface
- 661 materials. Appl. Opt. 40, 4852–4862. https://doi.org/10.1364/AO.40.004852
- 662 Laukamp, C., Cudahy, T., Cleverley, J.S., Oliver, N.H.S., Hewson, R., 2011. Airborne hyperspectral imaging of
- 663 hydrothermal alteration zones in granitoids of the Eastern Fold Belt, Mount Isa Inlier, Australia. Geochem. Explor.
- 664 Environ. Anal. 11, 3–24. https://doi.org/10.1144/1467-7873/09-231
- 665 Laukamp, C., Rodger, A., LeGras, M., Lampinen, H., Lau, I.C., Pejcic, B., Stromberg, J., Francis, N., Ramanaidou, E., 2021.
- 666 Mineral Physicochemistry Underlying Feature-Based Extraction of Mineral Abundance and Composition from
- Shortwave, Mid and Thermal Infrared Reflectance Spectra. Minerals 11, 347. https://doi.org/10.3390/min11040347
- 668 Lee, J., Cook, O.J., Argüelles, A.P., Mehmani, Y., 2023. Imaging geomechanical properties of shales with infrared light. Fuel
- 334, 126467. https://doi.org/10.1016/j.fuel.2022.126467
- 670 Leight, C.J., Ytsma, C., McCanta, M.C., Dyar, M.D., Glotch, T.D., 2024. Compositional Characterization of Glassy Volcanic
- 671 Material From VSWIR and MIR Spectra Using Partial Least Squares Regression Models. Earth Space Sci. 11,
- 672 e2023EA003439. https://doi.org/10.1029/2023EA003439
- 673 Leiter, S., Russell, J.K., Heap, M.J., Barendregt, R.W., Wilson, S., Edwards, B., 2024. Distribution, intensity, and timing of
- 674 palagonitization in glaciovolcanic deposits, Cracked Mountain volcano, Canada. Bull. Volcanol. 86, 32.
- 675 https://doi.org/10.1007/s00445-024-01724-w
- 676 Lewicka, E., Guzik, K., Galos, K., 2021. On the Possibilities of Critical Raw Materials Production from the EU's Primary
- 677 Sources. Resources 10, 50. https://doi.org/10.3390/resources10050050
- 678 Loche, M., Scaringi, G., Blahůt, J., Melis, M.T., Funedda, A., Da Pelo, S., Erbì, I., Deiana, G., Meloni, M.A., Cocco, F.,
- 679 2021. An Infrared Thermography Approach to Evaluate the Strength of a Rock Cliff. Remote Sens. 13, 1265.
- 680 https://doi.org/10.3390/rs13071265
- 681 Lund, J.W., Toth, A.N., 2021. Direct utilization of geothermal energy 2020 worldwide review. Geothermics 90, 101915.
- 682 https://doi.org/10.1016/j.geothermics.2020.101915
- 683 Lundberg, S., Lee, S.-I., 2017. A Unified Approach to Interpreting Model Predictions.
- 684 https://doi.org/10.48550/arXiv.1705.07874

- 685 Lyon, R.J.P., 1965. Analysis of rocks by spectral infrared emission (8 to 25 microns). Econ. Geol. 60, 715-736.
- 686 https://doi.org/10.2113/gsecongeo.60.4.715
- 687 Mineo, S., Pappalardo, G., 2016. The Use of Infrared Thermography for Porosity Assessment of Intact Rock. Rock Mech.
- 688 Rock Eng. 49, 3027–3039. https://doi.org/10.1007/s00603-016-0992-2
- 689 Mordensky, S.P., Villeneuve, M.C., Farquharson, J.I., Kennedy, B.M., Heap, M.J., Gravley, D.M., 2018. Rock mass
- 690 properties and edifice strength data from Pinnacle Ridge, Mt. Ruapehu, New Zealand. J. Volcanol. Geotherm. Res. 367,
- 691 46–62. https://doi.org/10.1016/j.jvolgeores.2018.09.012
- 692 Mustard, J.F., Hays, J.E., 1997. Effects of Hyperfine Particles on Reflectance Spectra from 0.3 to 25 µm. Icarus 125,
- 693 145–163. https://doi.org/10.1006/icar.1996.5583
- 694 Osterloo, M.M., Hamilton, V.E., Anderson, F.S., 2012. A laboratory study of the effects of roughness on the thermal infrared
- spectra of rock surfaces. Icarus 220, 404–426. https://doi.org/10.1016/j.icarus.2012.04.020
- 696 Poganj, A., Heap, M.J., Baud, P., 2025. Spatial distribution of alteration and strength in a lava dome: Implications for
- large-scale volcano stability modelling. J. Volcanol. Geotherm. Res.
- 698 Pola, A., Crosta, G., Fusi, N., Barberini, V., Norini, G., 2012. Influence of alteration on physical properties of volcanic rocks.
- Tectonophysics 566–567, 67–86. https://doi.org/10.1016/j.tecto.2012.07.017
- 700 Portela, B., Sepp, M.D., van Ruitenbeek, F.J.A., Hecker, C., Dilles, J.H., 2021. Using hyperspectral imagery for
- 701 identification of pyrophyllite-muscovite intergrowths and alunite in the shallow epithermal environment of the Yerington
- 702 porphyry copper district. Ore Geol. Rev. 131, 104012. https://doi.org/10.1016/j.oregeorev.2021.104012
- 703 Rost, E., Hecker, C., Schodlok, M.C., Van der Meer, F.D., 2018. Rock Sample Surface Preparation Influences Thermal
- 704 Infrared Spectra. Minerals 8, 475. https://doi.org/10.3390/min8110475
- 705 Salisbury, J.W., Eastes, J.W., 1985. The effect of particle size and porosity on spectral contrast in the mid-infrared. Icarus 64,
- 706 586–588. https://doi.org/10.1016/0019-1035(85)90078-8
- 707 Salisbury, J.W., Wald, A., 1992. The role of volume scattering in reducing spectral contrast of reststrahlen bands in spectra of
- 708 powdered minerals. Icarus 96, 121–128. https://doi.org/10.1016/0019-1035(92)90009-V
- 709 Schaefer, L.N., Kereszturi, G., Kennedy, B.M., Villeneuve, M., 2023. Characterizing lithological, weathering, and
- 710 hydrothermal alteration influences on volcanic rock properties via spectroscopy and laboratory testing: a case study of
- 711 Mount Ruapehu volcano, New Zealand. Bull. Volcanol. 85, 43. https://doi.org/10.1007/s00445-023-01657-w
- 712 Schaefer, L.N., Kereszturi, G., Villeneuve, M., Kennedy, B., 2021. Determining physical and mechanical volcanic rock
- 713 properties via reflectance spectroscopy. J. Volcanol. Geotherm. Res. 420, 107393.
- 714 https://doi.org/10.1016/j.jvolgeores.2021.107393
- 715 Schodlok, M.C., Whitbourn, L., Huntington, J., Mason, P., Green, A., Berman, M., Coward, D., Connor, P., Wright, W.,
- Jolivet, M., Martinez, R., 2016. HyLogger-3, a visible to shortwave and thermal infrared reflectance spectrometer system
- for drill core logging: functional description. Aust. J. Earth Sci.

- 718 Shapley, L.S., 1973. On Balanced Games without Side Payments, in: Hu, T.C., Robinson, S.M. (Eds.), Mathematical
- 719 Programming. Academic Press, pp. 261–290. https://doi.org/10.1016/B978-0-12-358350-5.50012-9
- 720 Simpson, M.P., Rae, A.J., 2018. Short-wave infrared (SWIR) reflectance spectrometric characterisation of clays from
- 721 geothermal systems of the Taupō Volcanic Zone, New Zealand. Geothermics 73, 74–90.
- 722 https://doi.org/10.1016/j.geothermics.2018.01.006
- 723 Soltani, M., Moradi Kashkooli, F., Dehghani-Sanij, A.R., Nokhosteen, A., Ahmadi-Joughi, A., Gharali, K., Mahbaz, S.B.,
- 724 Dusseault, M.B., 2019. A comprehensive review of geothermal energy evolution and development. Int. J. Green Energy
- 725 16, 971–1009. https://doi.org/10.1080/15435075.2019.1650047
- 726 Strehlow, K., Gottsmann, J.H., Rust, A.C., 2015. Poroelastic responses of confined aguifers to subsurface strain and their use
- for volcano monitoring. Solid Earth 6, 1207–1229. https://doi.org/10.5194/se-6-1207-2015
- 728 Swanson, E., Wilson, J., Broome, S., Sussman, A., 2020. The Complicated Link Between Material Properties and
- Microfracture Density for an Underground Explosion in Granite. J. Geophys. Res. Solid Earth 125, e2020JB019894.
- 730 https://doi.org/10.1029/2020JB019894
- 731 Takemura, T., Golshani, A., Oda, M., Suzuki, K., 2003. Preferred orientations of open microcracks in granite and their
- 732 relation with anisotropic elasticity. Int. J. Rock Mech. Min. Sci. 40, 443-454.
- 733 https://doi.org/10.1016/S1365-1609(03)00014-5
- 734 Thiele, S.T., Bnoulkacem, Z., Lorenz, S., Bordenave, A., Menegoni, N., Madriz, Y., Dujoncquoy, E., Gloaguen, R., Kenter,
- 735 J., 2022. Mineralogical Mapping with Accurately Corrected Shortwave Infrared Hyperspectral Data Acquired Obliquely
- 736 from UAVs. Remote Sens. 14, 5. https://doi.org/10.3390/rs14010005
- 737 Thiele, S.T., Grose, L., Samsu, A., Micklethwaite, S., Vollgger, S.A., Cruden, A.R., 2017. Rapid, semi-automatic fracture
- and contact mapping for point clouds, images and geophysical data. Solid Earth 8, 1241.
- 739 Thiele, S.T., Kirsch, M., Lorenz, S., Saffi, H., El Alami, S., Contreras Acosta, I.C., Madriz, Y., Gloaguen, R., 2024.
- Maximising the value of hyperspectral drill core scanning through real-time processing and analysis. Front. Earth Sci. 12.
- 741 https://doi.org/10.3389/feart.2024.1433662
- 742 Thiele, S.T., Lorenz, S., Kirsch, M., Acosta, I.C.C., Tusa, L., Hermann, E., Möckel, R., Gloaguen, R., 2021. Multi-scale,
- 743 multi-sensor data integration for automated 3-D geological mapping using hylite. Ore Geol. Rev. 136.
- 744 https://doi.org/10.1016/j.oregeorev.2021.104252
- 745 Tramontini, M., Rosas-Carbajal, M., Heap, M.J., Besson, P., Marteau, J., García, S., Zyserman, F.I., 2025. The effects of
- 746 hydrothermal alteration in the upper edifice of Copahue volcano (Argentina-Chile). Presented at the IAVCEI Conference,
- 747 Geneva.
- 748 Vairé, E., Heap, M.J., Baud, P., van Wyk de Vries, B., 2024. Quantifying the physical and mechanical heterogeneity of
- 749 porous volcanic rocks from the Chaîne des Puys (Massif Central, France). Bull. Volcanol. 86, 49.
- 750 https://doi.org/10.1007/s00445-024-01742-8

- 751 van der Meer, F., Kopačková, V., Koucká, L., van der Werff, H.M.A., van Ruitenbeek, F.J.A., Bakker, W.H., 2018.
- 752 Wavelength feature mapping as a proxy to mineral chemistry for investigating geologic systems: An example from the
- 753 Rodalquilar epithermal system. Int. J. Appl. Earth Obs. Geoinformation 64, 237–248.
- 754 https://doi.org/10.1016/j.jag.2017.09.008
- 755 Vincent, R.K., Hunt, G.R., 1968. Infrared Reflectance from Mat Surfaces. Appl. Opt. 7, 53-59.
- 756 https://doi.org/10.1364/AO.7.000053
- 757 Vrakas, A., Dong, W., Anagnostou, G., 2018. Elastic deformation modulus for estimating convergence when tunnelling
- through squeezing ground. Géotechnique 68, 713–728. https://doi.org/10.1680/jgeot.17.P.008
- 759 Williams, D.B., Ramsey, M.S., 2024. Infrared spectroscopy of volcanoes: from laboratory to orbital scale. Front. Earth Sci.
- 760 12. https://doi.org/10.3389/feart.2024.1308103
- 761